

Observational Signatures and Constraints on the Intermediate Neutron-Capture Process

The Case of the CEMP star TYC 6044–714–1 (RAVE J094921.8-161722)

R. E. Giribaldi¹, D. Vescovi^{2,3}, L. Magrini¹, S. Cristallo^{2,3}, V. D’Orazi⁴, L. Piersanti^{2,3}, D. Cornejo Espinoza⁵, S. Randich¹, and M. Baratella⁶

¹ INAF – Osservatorio Astrofisico di Arcetri, Largo E. Fermi 5, 50125 Firenze, Italy

² INAF – Osservatorio Astronomico d’Abruzzo, Via M. Maggini, 64100 Teramo, Italy

³ INFN - Sezione di Perugia, Via A. Pascoli, 06123 Perugia, Italy

⁴ Department of Physics, University of Rome Tor Vergata, via della Ricerca Scientifica 1, 00133 Roma, Italy

⁵ Escuela Nacional de Estudios Superiores Unidad Morelia, Universidad Nacional Autónoma de México, Morelia, 58190, México

⁶ ESO - European Southern Observatory, Alonso de Cordova, 3107, Vitacura, Santiago, Chile
e-mail: riano.escategiribaldi@inaf.it

Received / Accepted

ABSTRACT

Context. Observational abundances of Carbon Enhanced Metal-Poor (CEMP) stars with patterns in between those produced by the rapid (r-) and slow (s-) nucleosynthesis processes (CEMP-rs stars) are currently invoked as evidence of synthesis via the intermediate (i-) process in the early AGB evolutionary phase of metal-poor low mass stars. Nevertheless, discriminating between r+s- and i-process hypotheses requires high-precision abundances obtained through advanced spectral modelling techniques. Theoretical models of the i-process have become more robust, incorporating refined stellar modelling and nuclear reaction physics, providing ranges of probable elemental abundances and isotopic ratios predictions to be confronted with observational determinations.

Aims. We performed a new analysis of a high resolution and high signal-to-noise UVES spectrum of TYC 6044-714-1, one of the best studied CEMP-rs stars.

Methods. We derived accurate effective temperature (T_{eff}) and highly precise atmospheric parameters, element abundances, and isotopic ratios using state-of-the-art 1D non-LTE and 3D non-LTE spectral line modelling. Using the latest AGB nucleosynthesis models computed with FuNS evolutionary code, we assessed the possibility of the i-process to act aside the s-process.

Results. We find that TYC 6044-714-1 was likely born as a normal in-situ halo star about 13 Gyr ago, pre-enriched by the r-process through a standard Galactic chemical-evolution pathway. Among the explored scenarios, the s+r model provides the best overall reproduction of the observed heavy-element abundance pattern and Ba isotopic ratios, yielding excellent agreement across all three s-process peaks. While i+s+r models with increasing overshooting efficiency improve the fit for specific elements—particularly Nb and those between the first and second neutron-capture peaks—they do not consistently reproduce the full abundance pattern.

Conclusions. Although the i+s+r models achieve statistical fits comparable to the s+r case, they require extreme and physically implausible conditions, and predict s-process Ba fractions inconsistent with those inferred from isotopic ratios of the 4934 Å resonance line. We therefore conclude that the pure s+r scenario is the most plausible explanation.

Key words. stars: abundances – stars: atmospheres – stars:Population II – Galaxy: halo – nuclear reactions, nucleosynthesis, abundances – stars: AGB

1. Introduction

The synthesis of elements heavier than iron in stars is governed by neutron-capture processes, primarily classified as the slow (s-) and rapid (r-) processes, depending on the relative timescales of neutron captures and β -decays. However, observations of certain stellar populations and presolar grains reveal abundance patterns that cannot be fully explained by either of these canonical processes, pointing to the existence of an intermediate neutron-capture process, or i-process (Cowan & Rose 1977). The i-process occurs under neutron densities between those characteristic of the s- and r-processes, typically $10^{13} - 10^{15} \text{ cm}^{-3}$ (e.g. Banerjee et al. 2018; Clarkson et al. 2018), producing a distinct nucleosynthetic signature.

Proposed sites for i-process nucleosynthesis include He-shell flashes in low-metallicity asymptotic giant branch (AGB) stars,

proton ingestion events in early-generation stars, and rapidly accreting white dwarfs, among others; details of proposed scenarios are given in Choplin et al. (2021) and the literature within the paper. The study of the i-process has become increasingly important in the context of Galactic chemical evolution, as it has been invoked to explain anomalous abundance patterns. Carbon Enhanced Metal-Poor stars (CEMP¹, Beers & Christlieb 2005; Aoki et al. 2007) are prime candidates for hosting i-process material, as they frequently exhibit simultaneous enhancements of r- and s-process elements. In particular, based on moderately

¹ Defined as stars with $[\text{C}/\text{Fe}] > 0.7$ dex. This notation indicates a logarithmic scale of carbon $A(\text{C})$ relative to that of iron $A(\text{Fe})$ relative to the Sun. $A(\text{X})$ indicates that for a given element X, the logarithmic absolute abundance is defined as the number of atoms of element X per 10^{12} hydrogen atoms, $\log \epsilon(\text{X}) = A(\text{X}) \equiv \log_{10}(NX/NH) + 12.0$.

low-precision observational abundances of first peak (Sr, Y, and Zr) and heavy neutron-capture elements (from Ba to Hf), (Hampe et al. 2016) reported reasonable fits with i-process nucleosynthesis models. Further support is provided by the abundance pattern of BPS CS 31062-50 (Aoki et al. 2002; Johnson & Bolte 2004; Aoki et al. 2006; Lai et al. 2007), with moderately precise observational abundance measurements, has been announced as an evidence of the i-process nucleosynthesis by Wiedeking et al. (2025). However, CEMP stars are not the only candidates: signatures of the i-process have also been reported in a dwarf star with solar [C/Fe], based on abundances of light trans-iron elements ($32 \leq Z \leq 47$; Roederer et al. 2016).

The i-process pattern and the combination of the s- and r-processes signatures are difficult to discern. The task is performed by comparing observationally-based and theoretical patterns of heavy element-to-iron ratio versus atomic number Z . Among the heavy elements (i.e. those with $Z > 56$) detectable in spectra of CEMP stars, differences between the theoretical models do not exceed ~ 0.3 dex (e.g. Sbordone et al. 2020, Fig. 7). Therefore, accurate and precise abundance determinations are needed. This goal is often compromised by three factors: (i) the difficulty to derive accurate atmospheric parameters in CEMP stars, which mostly appear to be red giants, (ii) the lack of realistic 3D non-LTE line profile models for the majority of chemical elements, and (iii) spectra moderately crowded with carbon molecular features such as CH, CN, and C_2 , which totally or partially blend weak atomic features. Regarding (i), the reason is the limitation of custom methods. Namely, the excitation and ionization balance of Fe lines under 1D LTE is proven to strongly bias parameter determinations in very metal-poor stars ($[Fe/H] \lesssim -2$ dex). For instance, Ruchti et al. (2013); Giribaldi et al. (2023); Giribaldi & Smiljanic (2023) find typical biases of -300 K and -1.0 dex in T_{eff} and $\log g$, respectively. Colour-calibrations based on normal FGK stars underestimate T_{eff} by 100 to 500 K when applied to CEMP ones (e.g. Giribaldi et al. 2023, Fig. 10). Such biases are high enough to change true abundances in a heterogeneous way, affecting the diagnose of the dominant nucleosynthesis signature the star exhibits. Regarding (ii), only 1D non-LTE corrections are available for a few heavy elements. And even if available for all, there remains the fundamental issue of assessing how closely 1D non-LTE corrections recover the true abundances, particularly in giant stars. As a consequence, despite recent advances in modelling and observations, the frequency, astrophysical sites, and detailed yields of the i-process remain subjects of active investigation.

TYC 6044-714-1 is an ideal target for testing the i- and r+s-process hypothesis. It is a well-characterized CEMP-rs² star whose kinematics and chemical composition suggest an origin within the Milky Way halo about 13 gigayear (Gyr) ago (App. A and B). It orbits the Galactic centre in the opposite direction to the Sun and its binding energy is moderate. However, its [Mg/Fe] is compatible with the [Mg/Fe]-[Fe/H] signature of the most metal-poor tail of the Milky Way halo, which likely formed in situ (Giribaldi et al. 2025a); further details are provided in App. A. TYC 6044-714-1 (also known as RAVE J094921.8–161722) was identified as a CEMP-rs star by Sakari et al. (2018) and was determined to be compatible with an r+s-process signature by Gull et al. (2018). However, this

² Stars enhanced in neutron-capture elements that neither match the s- nor the r-processes alone. The rs notation implies $0 < [Ba/Eu] < 0.5$ dex according to Beers & Christlieb (2005), but classifications involving other elements and abundances ranges have been proposed by diverse authors.

Table 1. Spectral characteristics

Wavelength range [Å]	Obs. date	$R \equiv \lambda/\Delta\lambda$	S/N	RV [km/s]
TYC 6044-714-1 (Target)				
3282-4563	03/01/2025	65030	80	390.62 ± 0.13
3282-4563	07/01/2025	65030	70	389.72 ± 0.12
3282-4563	22/01/2025	65030	40	390.10 ± 0.14
4726-6834	03/01/2025	74450	270	390.76 ± 0.20
4726-6834	07/01/2025	74450	248	390.34 ± 0.20
4726-6834	22/01/2025	74450	184	390.64 ± 0.20
HD 186478 (Reference star)				
3304-4607	12/10/2000	40979	102	—
3304-4607	12/10/2000	40979	98	—
4654-6759	12/10/2000	42310	290	—

Notes. The last column indicates heliocentric velocity.

paradigm was recently challenged by Choplin et al. (2022a), who argued that a pure i-process occurring in a low-mass AGB star could explain the entire abundance pattern, including actinides.

In this work, we present new high-quality observations of TYC 6044-714-1, together with a detailed comparison to stellar evolution and nucleosynthesis models, with the aim of shedding new light on the role of the i-process in Galactic chemical evolution. The paper is organized as follows: Section 2 describes our observations and data reduction, Section 3 presents the determination of stellar parameters, Section 4 details the derivation of elemental abundances and isotopic ratios, and Section 5 provides theoretical predictions for the different neutron-capture channels. Finally, Section 6 discusses our results, and Section 7 summarizes our conclusions.

2. Observations and data reduction

We acquired spectra of TYC 6044-714-1 with the Ultraviolet and Visual Echelle Spectrograph (UVES, Dekker et al. 2000) mounted on the Very Large Telescope (VLT) of the European Southern Observatory (ESO). Three spectra in the blue and the red spectral regions were acquired using slit width $0.5''$ and binning 1×1 setup (data set ID 114.27JT.001 or 0114.B-0030(A), P.I. Giribaldi). The dates of acquisition, resolution $R = \lambda/\Delta\lambda$, and signal-to-noise (S/N) are listed in Table 1. The data were reduced to one-dimensional (1D) spectra and wavelength-calibrated using the Phase 3 pipeline (Arnaboldi et al. 2011). We corrected Doppler wavelength shifts by cross-correlating the spectra with a synthetic template from the iSPEC package (Blanco-Cuaresma et al. 2014), and computed heliocentric velocities using *astropy* routines; see values in Table 1. Our measurements are compatible with those compiled by Gull et al. (2018), hence no radial velocity variations are detected thus far, supporting the hypothesis of long period binary orbit or pole-on oriented system (e.g. Lucatello et al. 2005; Hansen et al. 2016). We co-added the spectra. The S/N ratio of the co-added spectrum was estimated in the blue and red regions using 14 and 12 pseudo-continuum ranges, respectively, resulting in $S/N = 140$ and $S/N = 430$.

In the analysis process, we used as reference the UVES archival spectra of the TITAN star HD186478 (Giribaldi et al. 2023), whose characteristics are listed in Table 2. Its revised parameters (Giribaldi et al. 2025a) are very similar to those of TYC6044-714-1, as reported in Table 2. The spectral processing followed exactly the same procedure as for TYC 6044-714-1.

3. Stellar atmospheric parameters

We determined the atmospheric parameters listed in Table 2 following the methodology outlined in Giribaldi et al. (2025a).

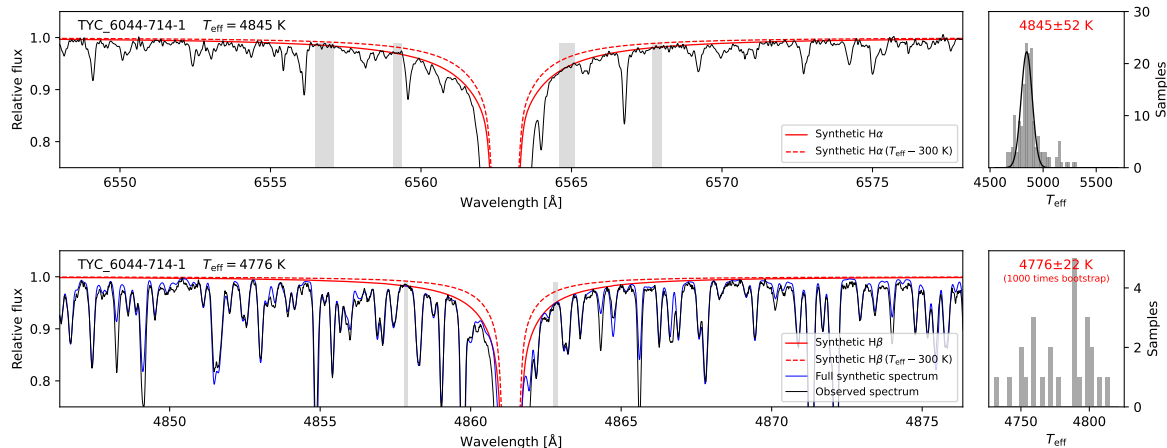


Fig. 1. Fits of the $H\alpha$ and $H\beta$ Balmer lines. The main plots show synthetic profiles (red solid line) fitted to the observational ones (black line). Synthetic lines from temperatures 300 K cooler than the determined ones are represented by the dashed red lines. Shades represent the fitting regions without metal and telluric line blends. The panels on the right display histograms of the temperatures associated to every pixel inside of the shaded regions in the left panels. In the top panel, the most likely temperature and its error are given by the median of the Gaussian profile fitted to the histogram and its σ dispersion. In the bottom panel, for robustness, the most likely temperature and its error are obtained by bootstrapping. A synthetic spectrum with molecular and atomic lines is represented in blue.

Table 2. Atmospheric parameters

Star	T_{eff} (K)	$\log g$ (dex)	$[\text{Fe}/\text{H}]_{\text{non-LTE}}$ (dex)	v_{mic} (km/s)
HD 186478	4793 ± 22	1.72 ± 0.15	-2.37 ± 0.09	1.94 ± 0.20
TYC 6044-714-1	4810 ± 41	1.70 ± 0.15	-2.17 ± 0.05	1.82 ± 0.04

Notes. Effective temperature is listed together with its total uncertainty. The uncertainty in $\log g$ corresponds to the range of values for which the slope of the trend in Fig. 2 remains within 1σ . Metallicity and v_{mic} are given with their internal uncertainties. We adopt the reference solar iron abundance $A(\text{Fe}) = 7.45$ dex from Lodders (2021). The T_{eff} value for HD 186478 is taken from Giribaldi et al. (2025a), whereas all other stellar parameters were re-derived in this work.

Briefly, effective temperature (T_{eff}) is retrieved by fitting the wings of the $H\alpha$ and $H\beta$ lines with the synthetic grids of Amarsi et al. (2018), produced with three-dimensional (3D) radiation-hydrodynamical model atmosphere simulations and considering departures from the local thermodynamic equilibrium (non-LTE). The normalization-fitting method of the observational profiles adopted in the present work is described in Giribaldi et al. (2019)³. The accuracy of the $H\alpha$ line model has been demonstrated in Giribaldi et al. (2021) and Giribaldi et al. (2023), showing no offset relative to the standard⁴, with a dispersion of about 50 K. The accuracy of the $H\beta$ line has not been systematically evaluated. Therefore, we determine T_{eff} from the $H\beta$ line relative to the reference star. The profile fits are shown in Fig. 1, where we also include the synthesis of molecular and atomic features for $H\beta$. The final temperature is obtained by averaging the values derived from $H\alpha$ and $H\beta$. Its error is given by the standard deviation of the mean (± 35 K) added in quadrature to the errors due to the uncertainties on surface gravity ($\log g$) and on metallicity ($[\text{Fe}/\text{H}]$) (these are ± 15 K each, according to Figs. 5 and 6 in Giribaldi et al. 2023).

Surface gravity and metallicity were derived by assuming the excitation equilibrium of Fe lines under 1D non-LTE assumption. An assessment of $\log g$ is presented in Sect. B. We apply line-by-line synthesis running the radiative transfer code Tur-

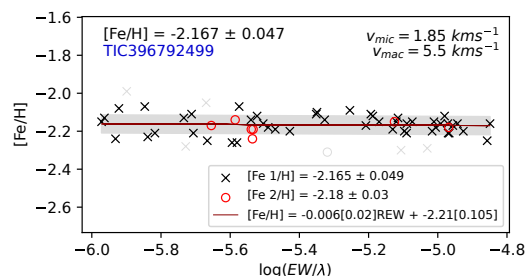


Fig. 2. Determination of metallicity and v_{mic} . Crosses and circles represent abundances from Fe I and Fe II lines, respectively. Gray symbols are clipped outliers. A regression of both species is represented by the red line, the coefficients of which and corresponding errors are given in the legends. The shade indicates the σ dispersion of the trend. Averages and standard deviations of Fe I and Fe II, individually, are also given in the legends.

bospectrum⁵ (Gerber et al. 2023) with MARCS model atmospheres (Gustafsson et al. 2008) considering the line list with atomic parameters in Heiter et al. (2021). We extracted iron departure coefficients based on the model atom developed in Bergemann et al. (2012) and Semenova et al. (2020). We applied the differential approach with respect to the reference star in order to optimise the $[\text{Fe}/\text{H}]$ precision; this method minimises the error related to the atomic parameters and normalization in twin stars (e.g. Meléndez et al. 2014). To ensure consistency, the spectra of the target star (TYC 6044-714-1) and the reference star (HD 186478) were analysed following the same procedure, adopting an identical line list and anchoring the normalisation to common pseudo-continuum points. For this latter step, we performed simultaneous local normalizations relative to a synthetic spectrum generated using the atmospheric parameters of the reference star and the abundances reported in Gull et al. (2018). We also avoided using Fe lines blended with molecular features by compiling an adapted line list based on the Fe line compilations from Giribaldi et al. (2025b), created through simultaneous visual inspection of the reference star and target spectra. Our final Fe line list is provided on Zenodo⁶.

³ Profile fitting code available at <https://github.com/RGiribaldi/Balmer-profile-fitting>

⁴ Set by the T_{eff} values of the Gaia Benchmark stars (Heiter et al. 2015) inferred via interferometry and the Infrared Flux Method (IRFM).

⁵ https://github.com/bertrandplez/Turbospectrum_NLTE

⁶ <https://doi.org/10.5281/zenodo.20159108>.

For both the reference and target stars, we applied spectral synthesis fixing T_{eff} and $\log g$ to the values in Table 2. We fixed the projected rotational velocity to 0 km s^{-1} , and allowed the microturbulence (v_{mic}) and the macroturbulence (v_{mac}) to vary freely. For the reference star, we set an $[\alpha/\text{Fe}]$ enhancement of $+0.35$ (Giribaldi et al. 2025a); whereas for the latter we set $[\alpha/\text{Fe}] = +0.25$ according to a preliminary Mg abundance determination, obtained considering the 1D non-LTE corrections in Fig. 6 of Giribaldi et al. (2025a). Our 1D non-LTE determination presented in Sec. 4 further validated this value. We constrained the most likely $[\text{Fe}/\text{H}]$ by requiring the absence of correlation between $[\text{Fe}/\text{H}]$ and the reduced equivalent width $\text{REW} = \log(EW/\lambda)^7$. We set the REW limit to values lower than -4.8 to exclude excessively saturated lines. Figure 2 shows the outcome of our differential analysis.

Following the results of Giribaldi et al. (2025b), we derived the v_{mic} value in Table 2 by averaging the values obtained from 1D non-LTE analysis and from the $T_{\text{eff}}-\log g$ -dependent relation of Dutra-Ferreira et al. (2016), which is based on 3D model atmospheres. The individual estimates are $1.85 \pm 0.07 \text{ km s}^{-1}$ for the former and $1.78 \pm 0.05 \text{ km s}^{-1}$ for the latter.

4. Elemental abundances and isotopic ratios from spectral analysis

We derived elemental abundances by spectral synthesis using Turbospectrum with MARCS model atmospheres. We used the atomic parameters from Heiter et al. (2021) for lines between 4200 \AA and redder wavelength limit, while for lines at bluer wavelengths we relied on the VALD 3 database (Ryabchikova et al. 2015). For all elements except C, Ba, and Eu, the solar isotopic abundance fractions were kept fixed at their default values⁸.

We modelled the molecular bands using the following line lists: ^{12}CH and ^{13}CH (Masseron et al. 2014), $^{12}\text{C}^{14}\text{N}$ (Brooke et al. 2014), $^{12}\text{C}_2$ (Brooke et al. 2013), $^{12}\text{C}^{13}\text{C}$ (Ram et al. 2014), $^{13}\text{C}^{14}\text{N}$ (Snedden et al. 2014), and ^{24}MgH (Skory et al. 2003).

To derive elemental abundances we used the lists of Gull et al. (2018) and da Silva & Smiljanic (2025) as initial references. We performed a visual inspection comparing our observational spectrum with synthetic spectra searching for all possible detectable lines. Considering all elements, the median of the abundance error associated with the microturbulence uncertainty ($\sigma_{v_{\text{mic}}}$) is 0.01 dex. Ba and Yb are exceptions because their lines are saturated, their $\sigma_{v_{\text{mic}}}$ are 0.10 and 0.12 dex, respectively. We computed the total error budget by adding in quadrature the following sources: $\sigma_{v_{\text{mic}}}$, the dispersion of the line-by-line measurement (σ_{stat}) or the error related to the noise in case only one line is available, the error related to T_{eff} (σ_T), the error related to $\log g$ (σ_g), and the error related to $[\text{Fe}/\text{H}]$ ($\sigma_{[\text{Fe}/\text{H}]}$). The errors $\sigma_{v_{\text{mic}}}$, σ_T , σ_g , and $\sigma_{[\text{Fe}/\text{H}]}$ are computed by changing the corresponding parameters by their errors in Table 2. Figure D.3 shows the impact of typical parameter errors in the element abundances. Table 3 lists our abundances and the number of lines used. We provide the entire line list in Zenodo⁹. Errors related to line-by-line abundance dispersions and total ones are listed separately. Nb and Th abundance determinations are presented in Sect. C. The former is relevant for the discussion Sect. 6.

⁷ EW is the equivalent width in \AA and λ is the wavelength in \AA .

⁸ Corresponding to the solar-system isotopic abundances compiled by Böhlke et al. (2005), as specified in the Turbospectrum file `atomicweights.dat`.

⁹ <https://doi.org/10.5281/zenodo.20159609>

1D non-LTE corrections were applied when available. The adopted corrections for each element are listed in Table 3 and were obtained from the following sources: Si (Bergemann et al. 2013; Amarsi & Asplund 2017), Ca (Mashonkina et al. 2007), Ti (Bergemann 2011), Cr (Bergemann & Cescutti 2010), Mn (Bergemann & Gehren 2008), Co (Bergemann et al. 2010), Ni (Eitner et al. 2023), Zn (Sitnova et al. 2022), Sr (Mashonkina et al. 2022) and Pb and Th (Mashonkina et al. 2012). For Al, we employed 3D non-LTE corrections in Nordlander & Lind (2017). The online tools MPIA¹⁰ (Kovalev et al. 2018) and NLTE¹¹ (Koutsouridou et al. 2025) were used when interpolations are implemented. Otherwise, corrections are extracted from tables in the papers themselves. In the following sections, we provide details about the analysis of some specific elements that are more challenging or critical.

4.1. Abundances and isotopic ratios of carbon, nitrogen, and magnesium

We derived the carbon abundance using the atomic C I lines at 5052.145 and 5380.320 \AA , as well as the Swan $^{12}\text{C}_2$ band in the $5140\text{--}5166 \text{ \AA}$ region, which exhibits moderately weak molecular features. These diagnostics yielded $A(\text{C}) = 7.33, 7.27,$ and 7.25 dex, respectively. The CH G-band near 4300 \AA was not used in the final determination because its strong molecular features may introduce systematic biases. For reference, we obtain $A(\text{C}) = 7.12$ dex with that band. We determined the $^{12}\text{C}/^{13}\text{C}$ isotopic ratio using the molecular features in the $4155\text{--}4240 \text{ \AA}$ region, a section of which is shown in Fig. D.2. Nitrogen abundances were derived by fitting the CN bands at $3556\text{--}3590$ and $3787\text{--}3812 \text{ \AA}$, which yielded $A(\text{N}) = 6.53$ and 6.46 dex, respectively.

The internal errors of the C and N abundances correspond to flux variations caused by noise. The internal errors of the $^{12}\text{C}/^{13}\text{C}$ ratio were estimated from the dispersion of the results of the most prominent individual features (31 features were selected for this error estimate) within the specified wavelength range. Namely, we computed the average of the 25% – 50% and 75% – 50% quantiles. We derived magnesium as described in Sec. 4.1 of Giribaldi et al. (2025a), by averaging the outcomes of the fits of the the lines at 5528 and 5711 \AA , assuming 1D non-LTE departures in Bergemann et al. (2017); each line yields $A(\text{Mg}) = 5.63$ and 5.69 dex, respectively. We iterated the determination of the elemental abundances (including Fe) until we obtained consistent results.

4.2. Abundances and isotopic ratios of barium and europium

The barium abundance and its isotopic fractions were determined following Giribaldi et al. (in prep.), where the method was calibrated with 72 stars and validated with Galaxy evolution models. It consists on deriving $A(\text{Ba})$ via 1D LTE spectral synthesis of the subordinate lines at 6141.715 and 6496.900 \AA ; while deriving isotopic fractions from 1D non-LTE synthesis of the resonance line Ba II 4934 \AA fixing the $A(\text{Ba})$ from 1D LTE. The accurate $\log gf$ values from De Munshi et al. (2015); Dutta et al. (2016), as in Gallagher et al. (2020) are required.

Giribaldi et al in prep. shows that 1D LTE yields equivalent $A(\text{Ba})$ to prototype 3D non-LTE¹² calculations within 0.1 dex

¹⁰ https://nlte.mpia.de/gui-siuAC_secE.php

¹¹ <https://nlite.pythonanywhere.com/>

¹² Computed by the code Linfor3D (Steffen et al. 2023) <https://www.chetec-infra.eu/3dnlte/abundance-corrections/barium/>.

Table 3. Elemental abundances.

Z	Element	A(X)	[X/Fe]+cor	σ_{stat}	σ_{Tot}	N.
6	C I	7.30	1.00	0.03	0.06	2
6	$^{12}\text{C}_2$	7.25	0.98	0.02	0.07	2 b.
6	$^{12}\text{C}/^{13}\text{C}$	19*	—	5.4*	—	1 b.
7	N I	6.48	0.81	0.03	0.13	2 b.
8	O I	7.15	0.62	0.04	0.06	2
11	Na I	4.02	-0.06	0.06	0.07	4
12	Mg I	[5.66]	0.42 - 0.14	0.03	0.04	2
13	Al I	[4.20]†	-0.42 + 0.33†	0.04	0.13	1
14	Si I	[5.69]	0.24 + 0.10	0.08	0.08	3
20	Ca I	[4.42]	0.16 + 0.08	0.05	0.06	12
21	Sc I & II	1.13	0.14	0.04	0.09	6
22	Ti I	[2.99]	0.16 + 0.04	0.06	0.08	5
22	Ti II	[3.01]	0.22 + 0	0.01	0.05	2
23	V II	1.91	0.14	0.06	0.10	6
24	Cr I	[3.44]	-0.38 + 0.34	0.03	0.06	6
25	Mn I	[3.24]	-0.68 + 0.65	0.03	0.06	4
26	Fe I	[5.28]	—	0.05	0.07	69
26	Fe II	[5.28]	—	0.03	0.05	8
27	Co I	[3.05]	-0.18 + 0.41	0.12	0.13	8
28	Ni I	[4.08]	-0.13 + 0.15	0.04	0.06	4
30	Zn I	[2.53]	-0.01 + 0.14	0.04	0.06	1
38	Sr II	[1.00]	0.10 + 0.19	0.07	0.10	3
39	Y II	0.12	0.07	0.08	0.11	5
40	Zr II	0.72	0.30	0.06	0.10	10
41	Nb II	0.02	0.73	0.18	0.20	2
44	Ru I	0.13	0.54	0.04	0.10	4
46	Pd I	-0.16	0.44	0.20	0.22	1
56	Ba II	0.79	0.77	0.03	0.10	2
57	La II	-0.20	0.86	0.03	0.08	5
58	Ce II	0.20	0.78	0.02	0.08	4
59	Pr II	-0.61	0.83	0.02	0.09	2
60	Nd II	0.03	0.77	0.03	0.08	14
62	Sm II	-0.53	0.67	0.05	0.09	2
63	Eu II	[-1.19]	0.40 + 0.05	0.02	0.08	4
64	Gd II	-0.47	0.62	0.05	0.09	4
65	Tb II	-1.52	0.34	0.06	0.13	3
66	Dy II	-0.52	0.54	0.08	0.11	8
68	Er II	-0.60	0.64	0.10	0.14	7
70	Yb II	-0.02†	1.30	0.02	0.14	2
72	Hf II	-0.33	0.98	0.04	0.09	2
76	Os I	-0.42	0.34	0.20	0.33	1
77	Ir I	-0.46	0.32	0.06	0.14	1
82	Pb I	[1.35]	1.39 + 0.37	0.04	0.09	1
90	Th II	[-1.77]	0.28 + 0.09	$\pm_{0.29}^{0.18}$	$\pm_{0.32}^{0.23}$	1

Notes. The symbol † indicates an unreliable abundance derived from an intense line. The symbol * indicates isotopic fractions instead of element abundance. Fractions [X/Fe] are computed considering the solar photospheric abundances in [Asplund et al. \(2009\)](#); except for Mg, which adopts the solar value $A(\text{Mg})_{\odot} = 7.55$ dex of [Asplund et al. \(2021\)](#). Abundances A(X) within brackets indicate determinations that consider 1D non-LTE or 3D non-LTE corrections according to Sect. 4. Element-to-iron ratios [X/Fe] of the same elements are listed in 1D LTE along with their corresponding 1D non-LTE corrections. Although Mg and Eu are determined by line profile fitting under 1D non-LTE on the fly, their ratios with respect to iron under 1D LTE are listed for comparison. Last column indicates the number of features used to obtain the abundances. Numbers accompanied by "b." indicate wide wavelength bands. Errors related to line-by-line abundance dispersions (σ_{stat}) and total ones are listed in columns five and six. For Nb, the error related to noise is listed instead of σ_{stat} to account for likely noise-induced biases.

for every star (see also a test case in [Giribaldi et al. 2025b](#)). On the other hand, 1D non-LTE calculations applied to subordinate lines underestimate A(Ba) by -0.2 dex for the Sun ([Gallagher et al. 2020](#)), and by -0.3 to -0.4 dex for stars with $[\text{Ba}/\text{Fe}] > 0.3$ dex ([Giribaldi et al. in prep.](#)). Figure 3 shows the 1D LTE fits and the corresponding 1D non-LTE profiles, the latter are systematically deeper and would yield lower abundances.

Isotopic fractions were obtained using 1D non-LTE departure coefficients ([Gallagher et al. 2020](#)) and hyperfine-structure data in [Giribaldi et al. \(2025b\)](#). The best fit corresponds to an 89% s-process contribution (Figure 4). The main uncertainty

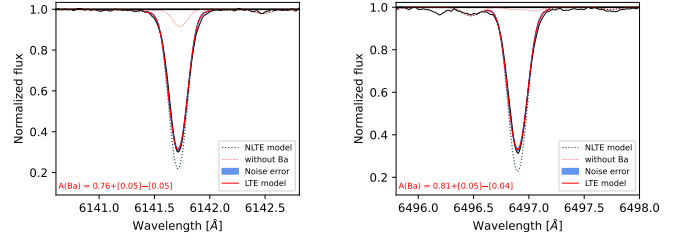


Fig. 3. Profile fits of Ba lines. The observed spectrum is shown in black, while the modelled line profiles in 1D LTE are colour-coded according to the legend. The associated abundances and noise-related uncertainties are indicated in each panel. 1D non-LTE line profiles synthesised with the same abundances obtained from 1D LTE fits are shown for comparison.

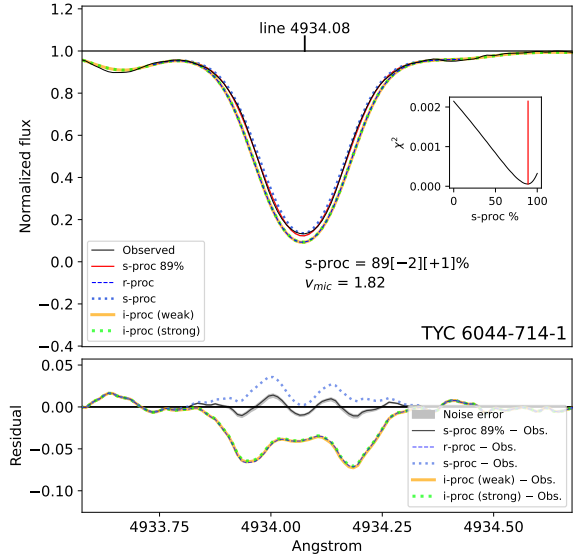


Fig. 4. Fit of the Ba resonance line at $\lambda 4934 \text{ \AA}$. *Top panel:* The observational profile is represented by the black line. The synthetic profile that best fit the observational profile is represented in red. Its isotopic ratio in terms of s-process percentage is noted in the plot along with its error due to the spectral noise. Synthetic profiles with isotopic ratio combinations in Table 4 are included as indicated in the legends. The inner plot shows the χ^2 related to the fit, where the determined percentage corresponding to the minimum χ^2 is represented by the bar. *Bottom panel:* The black line represents the difference between the best fit and the observational profile. The gray shade represents the noise error in terms of flux. Residuals of the r-, s-, and i-processes profiles minus the observational one are represented by the same line-style as in the top panel.

comes from T_{eff} (12% per 50 K), while flux noise and microturbulence have negligible impact. The remaining 11% of the abundance is attributed to the r-process, to the i-process, or a combined r+i contribution. From Table 3, the abundance fraction corresponding to the s-process is of $A(\text{Ba})_{s\text{-proc}} = 0.74$ dex, and the complement corresponding to r-, i-, or r+i- is of $A(\text{Ba})_{r/i\text{-proc}} = -0.17 \pm_{\infty}^{0.15}$ dex.

The europium abundance was determined under 1D non-LTE ([Storm et al. 2024](#)) from the lines at 4129.72 and 4205.03 Å, and under 1D LTE from the lines at 6437.64 and 6645 Å. For the lines at 4129.72 and 4205.03 Å, the HFS and its corresponding atomic parameters are taken from [da Silva & Smiljanic \(2025\)](#), while isotopic ratios related to the r- and i-processes are listed in Table 4. Both isotopic combinations produce nearly identical line profiles and equivalent abundances, see Fig. D.1.

Table 4. Isotopic ratios

Process	^{134}Ba	^{135}Ba	^{136}Ba	^{137}Ba	^{138}Ba
Slow	0.0081	0.0175	0.0558	0.0611	0.8586
Rapid	0.0000	0.4177	0.0000	0.3341	0.2482
Intermediate (weak)	0.0003	0.9296	0.0028	0.0374	0.0299
Intermediate (strong)	0.0001	0.7246	0.0077	0.1342	0.1334
Process	^{151}Eu	^{153}Eu			
Slow	0.4673	0.5327			
Rapid	0.5008	0.4992			
Intermediate (weak)	0.5291	0.4709			
Intermediate (strong)	0.5151	0.4849			

Notes. Quantities related the r -process are inferred from Prantzos et al. (2020). Quantities related to the s -process and i -process are inferred from a model of $1.5M_{\odot}$ with $[\text{Fe}/\text{H}] = -2.27$ dex (see Section 5); for the i -process, both a weak case ($f_{\text{top}} = 0.05$) and a strong case ($f_{\text{top}} = 0.15$, after the second PIE) are shown. For Ba, the contributions of ^{135}Ba and ^{137}Ba include the decay of ^{135}Cs and ^{137}Cs .

4.3. Prior Eu and Ba abundance enrichment of the binary system

Assuming that TYC 6044-714-1 became a CEMP star through binary interaction, it is reasonable to consider that, prior to its current evolutionary stage, it was a normal field star whose heavy-element composition reflected the Galactic r -process background. This assumption can be assessed observationally, independent of nucleosynthesis models, by comparing the Eu and Ba abundances of TYC 6044-714-1 with those of typical field stars at similar metallicity.

Figure 5 shows the distribution of $A(\text{Eu})$ as a function of $[\text{Fe}/\text{H}]$ for the TITAN stars (Giribaldi et al. 2021, 2023), including isotopic fractions from Giribaldi et al. (in prep.). TYC 6044-714-1 and the CEMP HD 196944 closely follow the trend defined by dwarf field stars (a similar trend was reported by Simmerer et al. 2004), indicating an r -process enrichment consistent with the general field-star population and showing no evidence of anomalous enhancement. The CEMP BPS CS 22892-052, and BPS CS 31082-001 (enhanced in barium) are clearly enriched in Eu. To further verify if the actinide content of TYC 6044-714-1 is consistent with this r -process background, we compared the Th abundance with the Eu estimate assuming a scaled solar r -process pattern. Adopting the r -process fractions from Prantzos et al. (2020), the expected solar r -process ratio is $A(\text{Th}/\text{Eu})_r \approx -0.35$. At the metallicity of TYC 6044-714-1, the field-star trend suggests $A(\text{Eu}) \approx -1.4$, which would correspond to an expected r -process baseline of $A(\text{Th}) \approx -1.75$. Our spectroscopic measurement for the star is $A(\text{Th}) = -1.77 \pm_{0.32}^{0.23}$. By accounting for radioactive decay over the system's age ($\approx +0.2$ dex), we derive an initial abundance of $A(\text{Th})_{\text{ini}} \approx -1.57 \pm_{0.32}^{0.23}$. This value is in good agreement with the predicted r -process models, considering the observational errors and the intrinsic scatter of Galactic r -process enrichment. The slight observed enhancement of Eu in TYC 6044-714-1 relative to the mean trend ($\approx +0.2$ dex) is separately explained by a combination of observational uncertainties (0.1 dex) and a minor s -process contribution from the AGB companion (see Sect. 5). Indeed, the accretion of $\approx 3\%$ of AGB material, which is intrinsically enriched in s -process europium ($[\text{Eu}/\text{Fe}]_{\text{agb}} \approx 1.3$), would shift the initial r -process Eu abundance by $\approx +0.1$ dex, without requiring an anomalous actinide-to-lanthanide ratio. These results confirm that the Th enrichment in this star follows a scaled-solar r -process distribution.

In the $A(\text{Ba})$ – $[\text{Fe}/\text{H}]$ plane (Fig. 6), TYC 6044-714-1 lies above the lower-envelope trend traced by dwarf stars, as seen for other CEMP stars and the Ba enhanced star BPS CS 31082-001 (Hill et al. 2002). At its metallicity, this trend corresponds to

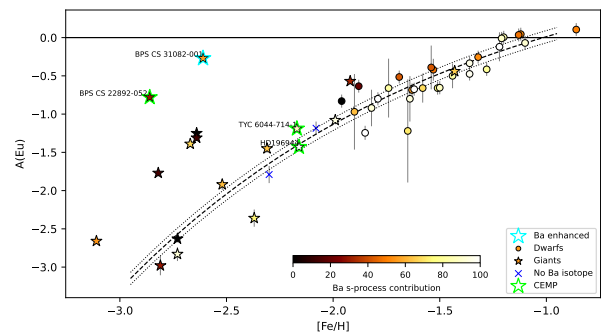


Fig. 5. $A(\text{Eu})$ versus $[\text{Fe}/\text{H}]$ of the TITAN stars. Dwarfs and giants are shown as circles and stars, respectively. The s -process contribution to the barium abundance, derived from isotopic ratios, is colour-coded as indicated by the colour bar. TYC 6044-714-1, other CEMP stars, and a star enhanced in barium are highlighted as indicated in the legend. Stars without Ba isotopic ratio measurement are represented by blue crosses. An exponential trend fitted to the dwarfs is shown by the dashed line, with its dispersion of $A(\text{Eu}) \pm 0.08$ dex indicated by the dotted lines.

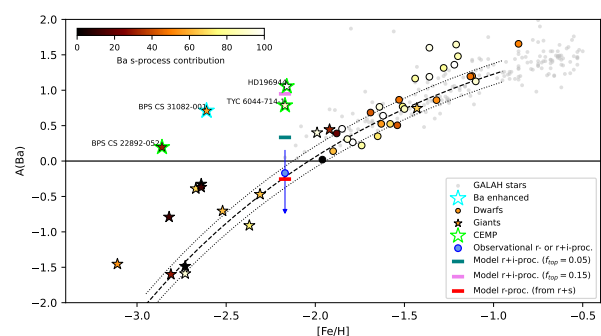


Fig. 6. $A(\text{Ba})$ versus $[\text{Fe}/\text{H}]$ of the TITAN stars. The elements of the plots are the same as in Fig. 5. Gray dots represent dwarf stars from the GALAH survey (Buder et al. 2021) and are shown for reference. The blue circle and its error bar indicate $A(\text{Ba})_{r/i-proc}$ according to the isotopic ratio analysis presented in Sect. 4.2. Ba abundances predicted by the nucleosynthesis models shown in Fig. 8, corresponding to the total barium abundance minus the s -process contribution (i.e., the r - or $r+i$ -process components), are indicated by the dashes according to the legends. An exponential trend fitted to the dwarf TITAN and GALAH stars is shown by the dashed line, with its dispersion of $A(\text{Ba}) \pm 0.15$ dex indicated by the dotted lines.

$A(\text{Ba}) = -0.25 \pm 0.15$ dex, which we adopt as a plausible estimate of the star's initial barium abundance. This baseline is consistent with the r -process contribution inferred from isotopic ratios (Sect. 4.2), $A(\text{Ba})_{r/i-proc} = -0.17 \pm_{\infty}^{+0.15}$ dex (blue point and error bar in the figure). Together, the Eu and Ba abundances, along with the Ba isotopic ratios, indicate that the pre-enrichment of TYC 6044-714-1 shows no evidence for abnormal nucleosynthetic enrichment prior to the binary interaction.

5. Nucleosynthesis modelling

In this section, we present our theoretical predictions for the s - and r -process contributions to the observed abundances and assess the possible presence of an i -process component. We compare our abundance results with a set of nucleosynthesis models varying contributions from the s -, i -, and r -processes.

5.1. AGB models

Most CEMP-s and CEMP-rs stars are found in binary systems (e.g. Lucatello et al. 2005; Hansen et al. 2016), thus their chem-

ical configurations are commonly interpreted as the outcome of mass-transfer events, in which material enriched in neutron-capture elements is accreted via stellar winds from a former AGB companion (e.g. [Masseron et al. 2010](#); [Bisterzo et al. 2010, 2011, 2012](#)). Therefore, the common practice is to compare their observed abundance patterns with those predicted for the nucleosynthetic yields of AGB stars.

Here, the observed abundance pattern of TYC 6044-714-1 is compared with theoretical AGB nucleosynthesis predictions computed using the FuNS evolutionary code ([Straniero et al. 2006](#); [Cristallo et al. 2009b](#); [Vescovi et al. 2021](#)). To model s-process nucleosynthesis, we adopt an extended nuclear network including nearly 500 isotopes connected by more than 800 nuclear reactions ([Vescovi 2021](#)). For the purposes of the present study, the network has been further expanded in order to properly follow the i-process nucleosynthesis path, resulting in a network comprising more than 1300 isotopes and 2500 reactions. The baseline nuclear network is extended by adopting neutron-capture reaction rates from the TENDL-astro 2023 database ([Rochman et al. 2025](#)) and from [Spyrou et al. \(2024\)](#) for the $^{139}\text{Ba}(n, \gamma)^{140}\text{Ba}$ reaction rate, while β -decay rates are taken from the NUBASE2020 evaluation ([Kondev et al. 2021](#)), complemented with theoretical rates from [Marketin et al. \(2016\)](#). Neutron-induced fission rates for trans-lead nuclei are from [Panov et al. \(2010\)](#).

During proton ingestion episodes (PIEs), the characteristic timescales of nuclear burning and convective transport become comparable (e.g., [Iwamoto et al. 2004](#)). As a consequence, nucleosynthesis and mixing equations are solved simultaneously in our calculations. A diffusive mixing scheme is adopted. We computed AGB models with an initial mass of $1.5M_{\odot}$ and a metallicity of $[\text{Fe}/\text{H}] = -2.27$ dex, scaling $A(\text{Fe})$ to the Solar iron abundance ([Lodders 2021](#)). The initial chemical composition assumes an α -enhancement of $[\text{O}/\text{Fe}] = 0.7$ dex and $[\alpha/\text{Fe}] = 0.4$ dex for the other α elements, consistent with the abundance patterns observed in low-metallicity Galactic halo stars (e.g., [Lind & Amarsi 2024](#)). According to current theoretical models, AGB stars of this mass and metallicity are not expected to experience PIEs, as the entropy barrier associated with the H-burning shell prevents efficient mixing between the He- and H-rich layers ([Fujimoto et al. 2000](#); [Iwamoto et al. 2004](#); [Cristallo et al. 2009a, 2016](#); [Choplin et al. 2022b](#)). Consistently, our standard models do not undergo PIEs and only experience s-process nucleosynthesis. In these models, the formation of the ^{13}C pocket is induced by magnetic buoyancy-driven mixing, following the prescription described in [Vescovi et al. \(2020, 2021\)](#). As expected for s-process nucleosynthesis at low metallicity, this results in strong lead production and significant enhancements of both the first ($[\text{ls}/\text{Fe}]^{13}$) and second s-process peaks ($[\text{hs}/\text{Fe}]^{14}$), with representative values of $[\text{ls}/\text{Fe}] = 1.49$ dex, $[\text{hs}/\text{Fe}] = 2.24$ dex, and $[\text{Pb}/\text{Fe}] = 3.37$ dex (see Fig. D.4)

However, the inclusion of additional extra mixing at the top of the convective thermal pulse can facilitate the occurrence of PIEs ([Choplin et al. 2024](#)). In stellar evolution calculations, such mixing is commonly described by assuming an exponential decay of the diffusion coefficient beyond the formal convective boundary, following

$$D_{\text{over}}(z) = D_{\text{cb}} \exp\left(-\frac{2z}{f_{\text{top}}H_{P,\text{cb}}}\right), \quad (1)$$

¹³ $[\text{ls}/\text{Fe}] = ([\text{Sr}/\text{Fe}] + [\text{Y}/\text{Fe}] + [\text{Zr}/\text{Fe}])/3$

¹⁴ $[\text{hs}/\text{Fe}] = ([\text{Ba}/\text{Fe}] + [\text{La}/\text{Fe}] + [\text{Ce}/\text{Fe}] + [\text{Pr}/\text{Fe}] + [\text{Nd}/\text{Fe}])/5$

where z is the distance from the convective boundary defined by the Schwarzschild criterion, D_{cb} and $H_{P,\text{cb}}$ are the diffusion coefficient and the local pressure scale height at the boundary, respectively, and f_{top} is a free parameter that controls the efficiency of the overshoot at the top of the convective thermal pulse. We find that, for a $1.5M_{\odot}$ model, adopting an overshooting parameter of $f_{\text{top}} = 0.05$ at the upper boundary of the convective thermal pulse is sufficient to trigger a PIE during the third thermal pulse, whereas lower values of f_{top} do not lead to proton ingestion. We also computed additional models with initial masses of 1 and $1.2M_{\odot}$ adopting the same overshooting efficiency ($f_{\text{top}} = 0.05$). These models do not show significant differences in either the occurrence of PIEs or the resulting nucleosynthetic signatures with respect to the $1.5M_{\odot}$ case. For this reason, in the following we focus on the $1.5M_{\odot}$ models, exploring the effects of varying the overshooting parameter at the top of the convective thermal pulse, considering values of $f_{\text{top}} = 0.05, 0.10,$ and 0.15 .

In all cases where a PIE occurs, the resulting nucleosynthesis is characterized by i-process conditions, with neutron densities exceeding 10^{15} cm^{-3} , intermediate between those typical of the s- and r-processes. After the PIE, the convective shell merges with the envelope, leading to a strong surface enrichment in heavy elements. For elements up to Ba, the resulting abundance patterns are broadly similar among the different f_{top} cases (see upper panel of Figure D.4). However, increasing the overshooting efficiency leads to a higher neutron exposure, with elements beyond Ba reaching very high surface overabundances. In particular, models with $f_{\text{top}} = 0.10$ and 0.15 are able to efficiently populate the Pb–Bi region. In these models, the nucleosynthetic flow also proceeds toward heavier nuclei to produce non-negligible amounts of actinides ([Choplin et al. 2022a](#)). For $f_{\text{top}} = 0.15$, two PIEs occur. While the first ingestion episode produces abundance patterns similar to those obtained for $f_{\text{top}} = 0.10$, the second PIE substantially enhances the neutron exposure, resulting in an even more efficient production of Pb and actinide nuclei.

In addition to heavy elements, large amounts of ^{12}C , ^{13}C , and ^{14}N are mixed into the envelope following a PIE. The enrichment in ^{12}C is mainly associated with the occurrence of a deep third dredge-up episode, which transports the products of 3α burning to the stellar surface. Conversely, ^{13}C and ^{14}N are produced by incomplete H burning within the H-rich convective shell formed during the ingestion event. The resulting increase in the CN abundance generally inhibits further proton ingestion events. The enhanced metallicity boosts the efficiency of H-shell burning in subsequent interpulse phases, strengthening the entropy barrier at the H/He interface and preventing the convective He-shell from penetrating into proton-rich regions during later thermal pulses. The star therefore resumes a standard AGB evolution, experiencing regular third dredge-up episodes and s-process nucleosynthesis during the following thermal pulses ([Cristallo et al. 2009a](#)). This behaviour is observed in the model with $f_{\text{top}} = 0.05$, which develops a single PIE. In this case, the final surface composition displays a genuinely mixed i+s chemical signature that can be approximately decomposed into two distinct contributions: elements lighter than Ba ($Z < 56$) are predominantly shaped by the i-process nucleosynthesis associated with the PIE, while heavier nuclei mainly reflect the subsequent s-process production (see lower panel of Figure D.4). The model with $f_{\text{top}} = 0.10$ also experiences a single PIE, but the substantially higher neutron exposure significantly alters the nucleosynthetic outcome, efficiently synthesizing heavy elements from Xe all the way through to the Pb peak. Consequently, the s-process contribution becomes secondary, and the final abundance pattern is predominantly determined by i-process nucleosynthesis across

the entire heavy-element range. For larger overshooting efficiencies, however, multiple PIE episodes may occur (Choplin et al. 2024). In particular, the model with $f_{\text{top}} = 0.15$ experiences a second PIE despite the prior CN enrichment of the envelope. As a consequence, the heavy-element nucleosynthesis is further enhanced by an additional i-process episode, leading to a final abundance pattern that is largely dominated by the i-process contribution over the whole mass range, including Pb and trans-lead elements. In both $f_{\text{top}} = 0.10$ and $f_{\text{top}} = 0.15$ models, the subsequent s-process nucleosynthesis during the late AGB phase has only a minor impact on the final surface composition.

5.2. Nucleosynthesis models versus measured abundances

To compare the chemical abundances of TYC 6044-714-1 with predictions from AGB models, we adopt a χ^2 fitting procedure. In particular, the model that best reproduces the observed abundances is identified by minimizing the reduced χ^2 value (χ_v^2), which quantifies the agreement between observations and theoretical predictions. The minimization is achieved by combining the material ejected by the AGB star with the envelope of the companion star. If m_{agb} denotes the mass accreted by the companion from the AGB ejecta and m_{com} the mass of the companion's envelope involved in the mixing, the resulting mass fraction of isotope i of element j , $X_{i,j}$, can be expressed as

$$X_{i,j} = X_{i,j}^{\text{agb}} d_{\text{agb}} + X_{i,j}^{\text{com}} (1 - d_{\text{agb}}), \quad (2)$$

where $X_{i,j}^{\text{agb}}$ and $X_{i,j}^{\text{com}}$ denote the isotopic mass fractions in the AGB ejecta and in the envelope of the companion star, respectively. The dilution factor is defined as $d_{\text{agb}} = m_{\text{agb}}/m_{\text{tot}}$, where the total mixed mass is $m_{\text{tot}} = m_{\text{agb}} + m_{\text{com}}$.

In principle, the initial composition of the companion star could be assumed to consist of pristine, α -enhanced material only. On the other hand, the presence of an additional pre-enrichment by a pure r-process contribution in the companion star can also be considered. In this more general case, Eq. 2 becomes

$$X_{i,j} = X_{i,j}^{\text{agb}} d_{\text{agb}} + X_{i,j}^{\text{r}} d_{\text{r}} + X_{i,j}^{\alpha} d_{\alpha}, \quad (3)$$

where $X_{i,j}^{\alpha}$ and $X_{i,j}^{\text{r}}$ denote the isotopic mass fractions associated with the α -enhanced pristine material and with the r-process component, respectively. The corresponding dilution factors are defined as $d_{\alpha} = m_{\alpha}/m_{\text{tot}}$ and $d_{\text{r}} = m_{\text{r}}/m_{\text{tot}}$, with the total mass now given by $m_{\text{tot}} = m_{\text{agb}} + m_{\alpha} + m_{\text{r}}$. By construction, the dilution factors satisfy $d_{\text{agb}} + d_{\alpha} + d_{\text{r}} = 1$.

The resulting overabundance of element j relative to iron is then expressed as

$$\left[\frac{X}{\text{Fe}} \right] = \log \left(\frac{X_j}{\text{Fe}} \right) - \log \left(\frac{X_j}{\text{Fe}} \right)_{\odot}, \quad (4)$$

where the elemental abundance X_j is obtained by summing over the individual isotopic mass fractions. Only elements heavier than Zn ($Z = 30$) are considered in the χ_v^2 calculation.

The s-process and mixed i+s models. We first compare pure s-process models with mixed i+s models in Figure 7. Among them, the best agreement with the observed abundance pattern is obtained for the i+s model with $f_{\text{top}} = 0.15$, which yields the lowest reduced χ^2 value. In particular, this model successfully reproduces the abundances of elements such as Eu and Gd,

which are severely underproduced in the pure s-process scenario and are known to receive a dominant contribution from the r-process (Prantzos et al. 2020). Despite this overall improvement, the i+s model still fails to reproduce the observed Th abundance, which remains underpredicted by about ~ 3 dex with respect to the measured value. It is important to note that the abundances of trans-lead elements are strongly affected by nuclear-physics uncertainties. In particular, Martinet et al. (2024) showed that correlated model uncertainties can induce surface abundance variations of up to ~ 3 dex for Th and U. However, even when considering these uncertainties in the most favourable case, the predicted actinide abundances remain only marginally consistent with the observations, which show $[\text{Th}/\text{Fe}] > 0$. For this comparison, the observed Th abundance has been increased by 0.2 dex to account for radioactive decay over a timescale of at least ~ 10 Gyr. Overall, this indicates that while a strong i-process contribution significantly improves the agreement for most heavy elements, an initial r-process enrichment is still required to fully account for the actinide abundances observed in TYC 6044-714-1.

The s-process and mixed i+s models with the r pre-enrichment. Figure 8 shows the comparison between the observed abundance pattern and the predictions obtained by combining AGB yields with an additional r-process contribution. In these models, the r-process input follows a scaled-solar distribution (Prantzos et al. 2020). This choice is justified by the observed universality of the main r-process for elements heavier than Ba in metal-poor stars (e.g., Sneden et al. 2008). Lighter r-elements can show variations (e.g., Hansen et al. 2012), but their impact on our fit is minimal as their abundances are primarily determined by the yields from the AGB companion. The absolute scale of the r-process component, d_{r} (Eq. 3), is treated as a free parameter optimized through a global χ^2 minimization including all measured elements with $Z > 30$. Although the fitting is performed over the entire heavy-element range, the value of d_{r} is principally constrained by those species with a significant r-process contribution, such as Eu, Gd, and the actinides (Th).

We consider the same set of AGB models discussed above, namely a pure s-process model (s+r) and three mixed i+s models with increasing overshooting efficiency ($f_{\text{top}} = 0.05, 0.10,$ and 0.15), all combined with an initial r-process enrichment (i+s+r). In these cases, the dilution factor associated with the AGB ejecta is denoted as d_{s} and $d_{\text{i+s}}$, respectively, while the r-process dilution factor d_{r} is treated as an independent free parameter.

For the mixed i+s models with $f_{\text{top}} = 0.10$ and 0.15 , the inclusion of an r-process component mainly affects the predicted actinide abundances, bringing Th into agreement with the observations, while the abundances of lighter neutron-capture elements remain almost unchanged. In contrast, for the model with $f_{\text{top}} = 0.05$, the addition of the r-process contribution leads to a substantial improvement not only for Th, but also for elements in the Eu–Er region, although Hf remains significantly underproduced. The pure s+r model also shows a marked improvement with respect to the s-only case, successfully reproducing the observed abundances of typical r-process tracers such as Eu and Gd, as well as the Th abundance. From a global perspective, the s+r model and the i+s+r model with $f_{\text{top}} = 0.15$ provide the best overall agreement with the observations, yielding comparable and significantly lower χ_v^2 values than the other cases.

Abundance percentages from different processes. Figure D.5 shows the elemental abundance fractions derived from

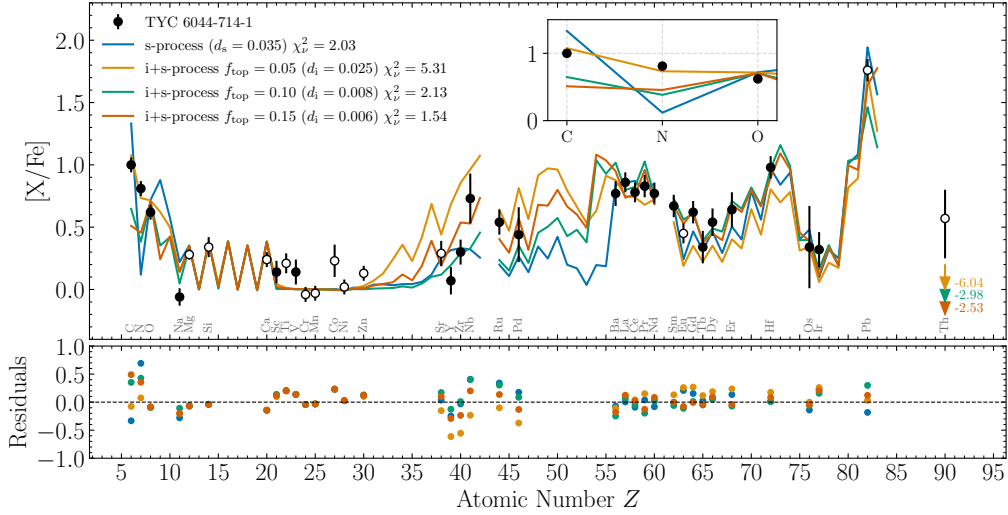


Fig. 7. *Upper panel:* Comparison between the observed abundance pattern of TYC 6044-714-1 and AGB nucleosynthesis predictions without an initial r-process enrichment. Observed abundances are shown as open white circles for elements corrected for non-LTE effects, and as filled black circles when corrections are not applied. Results for a s-process model (blue line) and for three mixed i+s models with $f_{\text{top}} = 0.05$ (yellow line), $f_{\text{top}} = 0.10$ (green line), and $f_{\text{top}} = 0.15$ (orange line), after dilution with the envelope of the companion star, are shown. The abundance has been increased by 0.2 dex to account for radioactive decay over ~ 10 Gyr (see text for details). The inset provides a zoom on the CNO region. The χ^2_{ν} values and the corresponding dilution factors are computed excluding Th, whose predicted abundance in the AGB models is virtually zero. *Lower panel:* Residuals between the observed and theoretically predicted abundance patterns, with symbol colours corresponding to the models shown in the upper panel. Residuals associated with the extra-mixing model are indicated by triangular symbols.

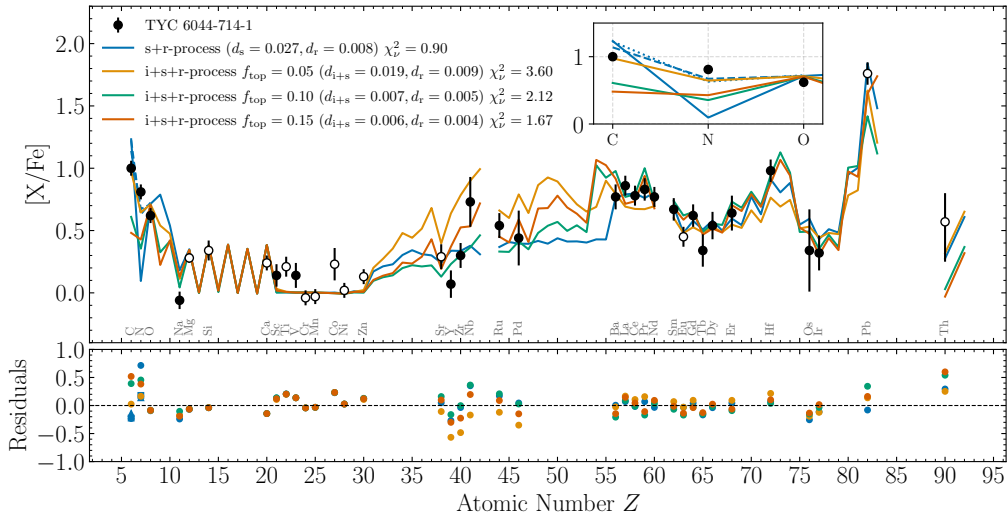


Fig. 8. *Upper panel:* Comparison between the observed abundance pattern of TYC 6044-714-1 and the best-fitting AGB nucleosynthesis models including an initial r-process enrichment. Observed abundances are shown as open white circles for elements corrected for non-LTE effects, and as filled black circles when corrections are not applied. Results for an s+r model (brown solid line) (blue line) and for three mixed i+s+r models with $f_{\text{top}} = 0.05$ (yellow line), $f_{\text{top}} = 0.10$ (green line), and $f_{\text{top}} = 0.15$ (orange line), after dilution with the envelope of the companion star, are shown. Additional models including extra mixing during the AGB (primary star) or the RGB (secondary star) phase are shown as a dashed and dotted blue curve (see the CN region in the $[X/\text{Fe}]$ distributions and the corresponding residuals), respectively. The r-process contribution is required to reproduce the Th abundance. *Lower panel:* Residuals between the observed and theoretically predicted abundance patterns, with symbol colours corresponding to the models shown in the upper panel. Residuals associated with the extra-mixing model are indicated by triangular (AGB) and square (RGB) symbols.

the nucleosynthesis models presented in Fig. 8. For barium, the s+r model predicts contributions of 96% and 4% from the s- and r-processes, respectively. For the mixed i+s+r models, the corresponding fractions are 31 + 65 + 4% for $f_{\text{top}} = 0.05$ and

90 + 9 + 1% for $f_{\text{top}} = 0.15$, reflecting the increasing dominance of the i-process contribution with stronger PIEs.

The observed $A(\text{Ba})_{r/i\text{-}proc}$ value (blue dot in Fig. 6) agrees with the s+r theoretical prediction, $A(\text{Ba}) = -0.26$ dex, obtained

by subtracting the s-process contribution from the total barium abundance (red dash in Fig. 6). When the i-process is included, the combined r+i contribution yields $A(\text{Ba}) = 0.33$ dex for $f_{\text{top}} = 0.05$ (green dash in Fig. 6) and $A(\text{Ba}) = 0.95$ dex for $f_{\text{top}} = 0.15$ (pink dash in Fig. 6).

Overall, the r+s-process model reproduces $A(\text{Ba})_{r/i\text{-}proc}$ accurately, whereas the r+i-process predictions fall outside the 1σ uncertainty.

6. Discussion

Our analysis yields stellar parameters and abundance patterns in excellent agreement with those reported by Gull et al. (2018). This similarity provides a consistent baseline to address the ongoing debate regarding the nucleosynthetic origin of the heavy elements in TYC 6044-714-1. While Choplin et al. (2022a) recently suggested a pure i-process origin for this star, our results support the original r+s interpretation by Gull et al. (2018). We encounter significant difficulties in reconciling a pure i-process or a mixed i+s-process scenario with the observed pattern and, crucially, with our new isotopic constraints. Among the explored scenarios, the s+r model yields the lowest reduced χ^2_v , providing an excellent fit to almost all elements across the three s-process peaks. The i+s+r models show a progressive improvement in the statistical quality of the fit as the overshooting efficiency increases, but they still present critical physical challenges.

In our calculations, which account for the α -enhancement typical of the Galactic halo at this metallicity and is consistent with the specific abundances observed in TYC 6044-714-1, we applied an extra-mixing (overshooting) at the upper border of the convective thermal pulse to trigger the proton ingestion and the i-process nucleosynthesis. Despite a systematic exploration of the overshooting efficiency (f_{top}), the resulting i+s+r models do not consistently improve the fit compared to the standard s+r scenario. Specifically, the $f_{\text{top}} = 0.05$ case performs significantly worse than the s+r model. Although it reproduces some elements between the first and second neutron-capture peaks, this comes at the cost of overproducing Y and Zr, and underproducing elements between La and Nd as well as Hf. The $f_{\text{top}} = 0.10$ model shows an improved χ^2_v relative to the $f_{\text{top}} = 0.05$ case, but it overestimates Ba and Eu while underestimating Pb and Th. The $f_{\text{top}} = 0.15$ model achieves a reduced χ^2_v comparable to the s+r case. This model solves several weaknesses of the lower overshooting scenarios: it reproduces Nb well and fits the Sr-Y-Zr region and the lanthanides satisfactorily, but it predicts a too low Th abundance. In addition, it predicts an i-process Ba fraction (90%, see Fig. D.5) that largely exceeds the observational one (11% at most) derived from isotopic ratios (Sect. 4.2).

Despite the statistical equivalence between the s+r and i+s+r $f_{\text{top}} = 0.15$ models, we consider the s+r interpretation more physically plausible. The $f_{\text{top}} = 0.15$ model requires extreme conditions, specifically a violent extra-mixing process at the thermal pulse border, making it a rather exotic scenario. The improved performance of the i+s+r models for Nb deserves particular attention, as this element benefits from the additional i-process contribution. However, no 1D non-LTE or 3D non-LTE corrections are available for Nb in the literature, so constraints from this element should be interpreted with caution. Overall, while including an i-process contribution improves the reproduction of some elements, it does not yield a better global fit than the s+r model. Overall, while we acknowledge the theoretical capability of the i-process to synthesize actinides under certain conditions (Choplin et al. 2022a), the complete chemical

signature of TYC 6044-714-1, including its isotopic composition, is much more consistently explained by mass transfer from an AGB companion dominated by standard s-process nucleosynthesis, superimposed on a pre-existing r-process enrichment.

A potential concern is whether the initial r-process enrichment of the birth cloud ($[r/\text{Fe}] \approx 0.4$ dex) could have impacted the nucleosynthesis in the primary AGB or the final pattern observed in the secondary. We find this effect negligible. In the primary AGB star, freshly synthesized material reaches intrinsic levels of $[\text{E}/\text{Fe}] \gtrsim 1.5$ dex, dominating over the initial r-seeds by more than an order of magnitude. Therefore, after strong dilution in the secondary ($d_{\text{agb}} \approx 0.03$), the s-process signature remains the only detectable contribution. The final chemical signature of TYC 6044-714-1 is thus a simple combination of the secondary's own birth-cloud r-process enrichment and the accreted s-process material.

Having discussed the heavy-element abundances, we now turn to the constraints provided by carbon and nitrogen. Under the simplified assumption that no extra-mixing processes operate, i+s+r models experiencing proton-ingestion episodes (PIEs) exhibit high C and N envelope abundances. In these models, the proton ingestion leads to local production of large amounts of ^{13}C and ^{14}N (Cristallo et al. 2009a; Choplin et al. 2021). Once this enriched material is mixed into the envelope, all models experiencing PIEs predict similarly low carbon isotopic ratios, $^{12}\text{C}/^{13}\text{C} \approx 4$, together with strong carbon and nitrogen enhancements ($\gtrsim 2.2$, see Figure 7). Subsequent standard TDU episodes progressively increase the surface ^{12}C abundance, raising the $^{12}\text{C}/^{13}\text{C}$ ratio while maintaining high C and N enhancements. This behaviour is common to the models with $f_{\text{top}} = 0.05, 0.10$, and 0.15 .

Models with larger overshooting parameters experience progressively stronger heavy-element enrichment during the PIEs. Although these models produce large absolute C and N enhancements, their C and N abundances are comparatively low relative to the neutron-capture elements, which dominate the χ^2 minimization. Consequently, when the dilution factor is set to reproduce the observed heavy-element abundances, carbon and nitrogen are over-diluted and underpredicted relative to observations. This effect becomes more pronounced for the $f_{\text{top}} = 0.10$ and 0.15 models. In this respect, the $f_{\text{top}} = 0.05$ model provides the best agreement, yielding C and N abundances closest to the observed values after dilution.

The pure s+r model, which does not experience PIEs, predicts much lower nitrogen enrichment and extremely high carbon isotopic ratios, with $^{12}\text{C}/^{13}\text{C}$ exceeding 8×10^3 . Nevertheless, low-mass stars ($\lesssim 2M_{\odot}$) are known to undergo extra-mixing processes during both the RGB and AGB phases (e.g., Gratton et al. 2000; Denissenkov & Vandenberg 2003; Nollett et al. 2003; Busso et al. 2010). Such processes can significantly lower $^{12}\text{C}/^{13}\text{C}$ and $[\text{C}/\text{Fe}]$, while increasing $[\text{N}/\text{Fe}]$, thereby improving agreement with the observed CN abundances. In the context of a binary system, such processes could have operated in the primary AGB donor, in the secondary star during its current RGB ascent (e.g., Placco et al. 2014), or as a combination of both.

To illustrate this, we computed two independent exploratory models. In the first case, following previous works (e.g., Abia et al. 2017), extra mixing was included only during the AGB phase of the primary star assuming a constant mixing velocity $v_{\text{mix}} = 100 \text{ cm s}^{-1}$ below the convective envelope, extending down to layers where the temperature reaches $T_{\text{mix}} = 36 \text{ MK}$. As a result, nitrogen abundance is enhanced, while the carbon isotopic ratio is lowered before the mass transfer occurs. Carbon elemental abundance is only slightly depleted. After dilution

with the companion's envelope, the resulting surface abundances are in good agreement with the observed values of TYC 6044-714-1 (see Fig. 8). In the second case, we modeled the internal evolution of the secondary star only ($0.8 M_{\odot}$), assuming extra-mixing ($v_{\text{mix}} = 1 \text{ cm s}^{-1}$, $T_{\text{mix}} = 23 \text{ MK}$) during the RGB phase, specifically after the luminosity bump. As shown in Fig. D.6, this second scenario effectively reprocesses the accreted carbon into nitrogen, matching the observed $[\text{N}/\text{Fe}]$ and $^{12}\text{C}/^{13}\text{C}$ values at the current evolutionary stage of TYC 6044-714-1 ($\log g \approx 1.7$). In this case, carbon remains slightly overproduced compared to observations due to the high carbon content originally predicted for the primary AGB. While we cannot uniquely determine whether the mixing occurred in the primary, the secondary, or both, these tests demonstrate that a modest amount of extra-mixing – a standard physical process in metal-poor giants – suffices to reproduce the observed CN abundances. Consequently, light elements do not provide a decisive diagnostic against the s+r scenario; on the contrary, i-process models with $f_{\text{top}} = 0.10$ and 0.15 are further disfavoured because they underpredict C and N after dilution. Since any subsequent extra-mixing would further reduce $[\text{C}/\text{Fe}]$ while increasing $[\text{N}/\text{Fe}]$, it would accentuate the discrepancy in these models, whereas it provides a consistent physical solution for the s+r case.

7. Summary and conclusion

We have analyzed the chemical abundances of the CEMP-rs star TYC 6044-714-1 using high-quality observations combined with detailed nucleosynthesis modelling. Among the explored scenarios, the s+r model provides the best overall fit, achieving the lowest reduced χ^2 , and reproducing the heavy-element pattern across all three s-process peaks. Although i+s+r models with increasing overshooting efficiency ($f_{\text{top}} = 0.05\text{--}0.15$) improve the fit for certain elements, particularly Nb and those between the first and second neutron-capture peaks, they generally fail to reproduce the full abundance pattern consistently. The $f_{\text{top}} = 0.15$ model achieves a statistical fit comparable to s+r, but requires extreme and physically unlikely conditions, making the pure s+r scenario more plausible. In addition, it predicts an s-process Ba fraction of 9%, which is inconsistent with the value of $89 \pm 12\%$ inferred from isotopic ratios.

Carbon and nitrogen abundances provide additional constraints. i+s+r models experiencing proton-ingestion episodes (PIEs) predict large absolute enhancements of C and N, but when diluted to match heavy-element abundances, they underpredict the observed C and N. Among these models, the $f_{\text{top}} = 0.05$ case yields the closest agreement with the observed CN abundances. In contrast, the s+r model, which does not include PIEs, predicts very high $^{12}\text{C}/^{13}\text{C}$ ratios and low N enrichment; however, the inclusion of modest extra-mixing processes during the AGB phase reproduces the observed C and N abundances, consistent with expectations for low-mass stars.

Overall, our results indicate that the chemical pattern of TYC 6044-714-1 is most consistently explained by mass transfer from an AGB companion dominated by s-process nucleosynthesis, superimposed on a pre-existing r-process enrichment from standard Galactic chemical-evolution. While the i-process may contribute to certain elements, its inclusion does not improve the global fit, and extreme i-process scenarios are disfavoured. Light elements alone cannot provide a decisive diagnostic, but the combination of heavy-element abundances and isotopic ratios supports a dominant s+r origin for this star's enrichment.

In stars with noisier blue spectra ($\lambda \lesssim 4800 \text{ \AA}$) or stronger blending from carbon features, the uncertainties in elemental

abundances may easily increase by a factor of two to three relative to those reported here. Under such conditions, discriminating between the s+r and i+s+r nucleosynthetic scenarios solely through comparisons between observed and model-predicted abundances becomes nearly impossible. We demonstrate that a careful analysis of the Ba II resonance line at 4934 \AA , aimed at determining the s-process contribution to the total barium abundance, can substantially improve the ability to discriminate between the nucleosynthetic processes responsible for the observed chemical pattern.

The UVES spectrum employed in this study closely reproduces the wavelength coverage and resolving power foreseen for HRMOS, a very high resolution spectrograph that will be proposed as a future instrument for the ESO VLT. It thus provides an empirical benchmark for assessing the expected performance of one of its proposed science cases (Magrini et al. 2023). Given that the current requirement for HRMOS is a multiplex capability of 50-80, this same analysis could in principle be extended to comparably large stellar samples in a single observational setup.

Acknowledgements. The authors thank A. Amarsi for discussions and support to the manuscript. The authors thank the anonymous referee for constructive criticism that significantly improved the quality of the paper. R.E.G. and L.M. acknowledge support from INAF through the Large Grants EPOCH and WST, funding for the WEAVE project, the Mini-Grants Checs (1.05.23.04.02), and financial support under the National Recovery and Resilience Plan (PNRR), Mission 4, Component 2, Investment 1.1, Call for tender No. 104 published on 2 February 2022 by the Italian Ministry of University and Research (MUR), funded by the European Union – NextGenerationEU, through the Project ‘Cosmic POT’ (Grant Assignment Decree No. 2022X4TM3H, MUR). D.V. and S.C. acknowledge funding by the European Union – NextGenerationEU RFF M4C2 1.1 PRIN 2022 project ‘2022RJLWHN URKA’ and by INAF 2023 Theory Grant ObFu 1.05.23.06.06 ‘Understanding R-process & Kilonovae Aspects’. L.P. acknowledges partial financial support from the INAF Minigrant 2023 Self-consistent Modeling of Interacting Binary Systems (1.05.23.04.02). Use was made of the Simbad database, operated at the CDS, Strasbourg, France, and of NASA's Astrophysics Data System Bibliographic Services. This publication makes use of data products from the Two Micron All Sky Survey, which is a joint project of the University of Massachusetts and the Infrared Processing and Analysis Center/California Institute of Technology, funded by the National Aeronautics and Space Administration and the National Science Foundation. This research used Astropy <http://www.astropy.org> a community-developed core Python package for Astronomy (Astropy Collaboration et al. 2018). This work presents results from the European Space Agency (ESA) space mission Gaia. Gaia data are processed by the Gaia Data Processing and Analysis Consortium (DPAC). Funding for the DPAC is provided by national institutions, in particular the institutions participating in the Gaia MultiLateral Agreement (MLA). The Gaia mission website is <https://www.cosmos.esa.int/gaia>. The Gaia archive website is <https://archives.esac.esa.int/gaia>. Based on observations made with ESO Telescopes at the La Silla Paranal Observatory under programme IDs 114.27JT.001 or 0114.B-0030(A) and 165.N-0276(A).

References

- Abia, C., Hedrosa, R. P., Domínguez, I., & Straniero, O. 2017, *A&A*, 599, A39
- Amarsi, A. M. & Asplund, M. 2017, *MNRAS*, 464, 264
- Amarsi, A. M., Nordlander, T., Barklem, P. S., et al. 2018, *A&A*, 615, A139
- Anders, E. & Ebihara, M. 1982, *Geochim. Cosmochim. Acta*, 46, 2363
- Aoki, W., Beers, T. C., Christlieb, N., et al. 2007, *ApJ*, 655, 492
- Aoki, W., Bisterzo, S., Gallino, R., et al. 2006, *ApJ*, 650, L127
- Aoki, W., Norris, J. E., Ryan, S. G., Beers, T. C., & Ando, H. 2002, *PASJ*, 54, 933
- Arnaboldi, M., Retzlaff, J., Slijkhuis, R., et al. 2011, *The Messenger*, 144, 17
- Asplund, M., Amarsi, A. M., & Grevesse, N. 2021, *A&A*, 653, A141
- Asplund, M., Grevesse, N., Sauval, A. J., & Scott, P. 2009, *ARA&A*, 47, 481
- Astropy Collaboration, Price-Whelan, A. M., Sipőcz, B. M., et al. 2018, *AJ*, 156, 123
- Bailer-Jones, C. A. L., Rybizki, J., Foesneau, M., Demleitner, M., & Andrae, R. 2021, *AJ*, 161, 147
- Banerjee, P., Qian, Y.-Z., & Heger, A. 2018, *ApJ*, 865, 120
- Beers, T. C. & Christlieb, N. 2005, *ARA&A*, 43, 531
- Belokurov, V., Erkal, D., Evans, N. W., Koposov, S. E., & Deason, A. J. 2018, *MNRAS*, 478, 611

- Belokurov, V., Sanders, J. L., Fattahi, A., et al. 2020, *MNRAS*, 494, 3880
- Bergemann, M. 2011, *MNRAS*, 413, 2184
- Bergemann, M. & Cescutti, G. 2010, *A&A*, 522, A9
- Bergemann, M., Collet, R., Amarsi, A. M., et al. 2017, *ApJ*, 847, 15
- Bergemann, M. & Gehren, T. 2008, *A&A*, 492, 823
- Bergemann, M., Kudritzki, R.-P., Würl, M., et al. 2013, *ApJ*, 764, 115
- Bergemann, M., Lind, K., Collet, R., Magic, Z., & Asplund, M. 2012, *MNRAS*, 427, 27
- Bergemann, M., Pickering, J. C., & Gehren, T. 2010, *MNRAS*, 401, 1334
- Bisterzo, S., Gallino, R., Straniero, O., Cristallo, S., & Käppeler, F. 2010, *MNRAS*, 404, 1529
- Bisterzo, S., Gallino, R., Straniero, O., Cristallo, S., & Käppeler, F. 2011, *MNRAS*, 418, 284
- Bisterzo, S., Gallino, R., Straniero, O., Cristallo, S., & Käppeler, F. 2012, *MNRAS*, 422, 849
- Blanco-Cuaresma, S., Soubiran, C., Heiter, U., & Jofré, P. 2014, *A&A*, 569, A111
- Böhlke, J. K., de Laeter, J. R., De Bièvre, P., et al. 2005, *Journal of Physical and Chemical Reference Data*, 34, 57
- Bonaca, A., Conroy, C., Wetzell, A., Hopkins, P. F., & Kereš, D. 2017, *ApJ*, 845, 101
- Bonifacio, P., Monaco, L., Salvadori, S., et al. 2021, *A&A*, 651, A79
- Brooke, J. S. A., Bernath, P. F., Schmidt, T. W., & Bacskay, G. B. 2013, *J. Quant. Spec. Radiat. Transf.*, 124, 11
- Brooke, J. S. A., Ram, R. S., Western, C. M., et al. 2014, *ApJS*, 210, 23
- Buder, S., Sharma, S., Kos, J., et al. 2021, *The GALAH+ survey: Third data release*
- Busso, M., Palmerini, S., Maiorca, E., et al. 2010, *ApJ*, 717, L47
- Casagrande, L., Lin, J., Rains, A. D., et al. 2021, *MNRAS*, 507, 2684
- Casagrande, L. & Vandenberg, D. A. 2018, *MNRAS*, 479, L102
- Choplin, A., Goriely, S., & Siess, L. 2022a, *A&A*, 667, L13
- Choplin, A., Siess, L., & Goriely, S. 2021, *A&A*, 648, A119
- Choplin, A., Siess, L., & Goriely, S. 2022b, *A&A*, 667, A155
- Choplin, A., Siess, L., Goriely, S., & Martinet, S. 2024, *A&A*, 684, A206
- Clarkson, O., Herwig, F., & Pignatari, M. 2018, *MNRAS*, 474, L37
- Cowan, J. J. & Rose, W. K. 1977, *ApJ*, 212, 149
- Cristallo, S., Karinkuzhi, D., Goswami, A., Piersanti, L., & Greife, D. 2016, *ApJ*, 833, 181
- Cristallo, S., Piersanti, L., Straniero, O., et al. 2009a, *PASA*, 26, 139
- Cristallo, S., Straniero, O., Gallino, R., et al. 2009b, *ApJ*, 696, 797
- Cutri, R. M., Skrutskie, M. F., van Dyk, S., et al. 2003, *2MASS All Sky Catalog of point sources*.
- da Silva, A. R. & Smiljanic, R. 2025, *A&A*, 696, A122
- De Munshi, D., Dutta, T., Rebhi, R., & Mukherjee, M. 2015, *Phys. Rev. A*, 91, 040501
- Dekker, H., D'Odorico, S., Kaufer, A., Delabre, B., & Kotzlwski, H. 2000, in *Society of Photo-Optical Instrumentation Engineers (SPIE) Conference Series*, Vol. 4008, *Optical and IR Telescope Instrumentation and Detectors*, ed. M. Iye & A. F. Moorwood, 534–545
- Denissenkov, P. A. & Vandenberg, D. A. 2003, *ApJ*, 593, 509
- Di Matteo, P., Haywood, M., Lehnert, M. D., et al. 2019, *A&A*, 632, A4
- Dutra-Ferreira, L., Pasquini, L., Smiljanic, R., Porto de Mello, G. F., & Steffen, M. 2016, *A&A*, 585, A75
- Dutta, T., de Munshi, D., Yum, D., Rebhi, R., & Mukherjee, M. 2016, *Scientific Reports*, 6, 29772
- Eitner, P., Bergemann, M., Ruitter, A. J., et al. 2023, *A&A*, 677, A151
- Fitzpatrick, E. L. 1999, *PASP*, 111, 63
- Fujimoto, M. Y., Ikeda, Y., & Iben, Jr., I. 2000, *ApJ*, 529, L25
- Gaia Collaboration, Brown, A. G. A., Vallenari, A., et al. 2018, *A&A*, 616, A1
- Gallagher, A. J., Bergemann, M., Collet, R., et al. 2020, *A&A*, 634, A55
- Gallart, C., Bernard, E. J., Brook, C. B., et al. 2019, *Nature Astronomy*, 3, 932
- Gerber, J. M., Magg, E., Plez, B., et al. 2023, *A&A*, 669, A43
- Giribaldi, R. E., da Silva, A. R., Smiljanic, R., & Cornejo Espinoza, D. 2021, *A&A*, 650, A194
- Giribaldi, R. E., Magrini, L., Rossi, M., et al. 2025a, *A&A*, 698, A11
- Giribaldi, R. E., Magrini, L., Schiappacasse-Ulloa, J., Randich, S., & Merle, T. 2025b, *A&A*, 702, A65
- Giribaldi, R. E. & Smiljanic, R. 2023, *A&A*, 673, A18
- Giribaldi, R. E., Ubaldo-Melo, M. L., Porto de Mello, G. F., et al. 2019, *A&A*, 624, A10
- Giribaldi, R. E., Van Eck, S., Merle, T., et al. 2023, *A&A*, 679, A110
- Gratton, R. G., Sneden, C., Carretta, E., & Bragaglia, A. 2000, *A&A*, 354, 169
- Gull, M., Frebel, A., Cain, M. G., et al. 2018, *ApJ*, 862, 174
- Gustafsson, B., Edvardsson, B., Eriksson, K., et al. 2008, *A&A*, 486, 951
- Hampel, M., Stancliffe, R. J., Lugaro, M., & Meyer, B. S. 2016, *ApJ*, 831, 171
- Hannaford, P., Lowe, R. M., Biemont, E., & Grevesse, N. 1985, *A&A*, 143, 447
- Hansen, C. J., Primas, F., Hartman, H., et al. 2012, *A&A*, 545, A31
- Hansen, T. T., Andersen, J., Nordström, B., et al. 2016, *A&A*, 588, A3
- Heiter, U., Jofré, P., Gustafsson, B., et al. 2015, *A&A*, 582, A49
- Heiter, U., Lind, K., Bergemann, M., et al. 2021, *A&A*, 645, A106
- Helmi, A., Babusiaux, C., Koppelman, H. H., et al. 2018, *Nature*, 563, 85
- Hill, V., Plez, B., Cayrel, R., et al. 2002, *A&A*, 387, 560
- Iwamoto, N., Kajino, T., Mathews, G. J., Fujimoto, M. Y., & Aoki, W. 2004, *ApJ*, 602, 377
- Jean-Baptiste, I., Di Matteo, P., Haywood, M., et al. 2017, *A&A*, 604, A106
- Johnson, J. A. & Bolte, M. 2004, *ApJ*, 605, 462
- Kondev, F. G., Wang, M., Huang, W. J., Naimi, S., & Audi, G. 2021, *Chinese Physics C*, 45, 030001
- Koppelman, H. H., Bos, R. O. Y., & Helmi, A. 2020, *A&A*, 642, L18
- Koppelman, H. H., Helmi, A., Massari, D., Price-Whelan, A. M., & Starkenburg, T. K. 2019, *A&A*, 631, L9
- Koutsouridou, I., Skúladóttir, Á., & Salvadori, S. 2025, *A&A*, 699, A32
- Kovalev, S., Brinkmann, M., Bergemann, M., & MPA IT-department. 2018, *NLTE MPA web server*, [Online]. Available: <http://nlte.mpa.de> Max Planck Institute for Astronomy, Heidelberg.
- Lai, D. K., Johnson, J. A., Bolte, M., & Lucatello, S. 2007, *ApJ*, 667, 1185
- Lind, K. & Amarsi, A. M. 2024, *ARA&A*, 62, 475
- Lindgren, L., Bastian, U., Biermann, M., et al. 2021, *A&A*, 649, A4
- Lodders, K. 2021, *Space Sci. Rev.*, 217, 44
- Lucatello, S., Gratton, R. G., Beers, T. C., & Carretta, E. 2005, *ApJ*, 625, 833
- Magrini, L., Bensby, T., Brucalassi, A., et al. 2023, *arXiv e-prints*, arXiv:2312.08270
- Marketin, T., Huther, L., & Martínez-Pinedo, G. 2016, *Phys. Rev. C*, 93, 025805
- Martinet, S., Choplin, A., Goriely, S., & Siess, L. 2024, *Astronomy and Astrophysics*, 684, A8
- Mashonkina, L., Korn, A. J., & Przybilla, N. 2007, *A&A*, 461, 261
- Mashonkina, L., Pakhomov, Y. V., Sitnova, T., et al. 2022, *MNRAS*, 509, 3626
- Mashonkina, L., Ryabtsev, A., & Frebel, A. 2012, *A&A*, 540, A98
- Massari, D., Koppelman, H. H., & Helmi, A. 2019, *A&A*, 630, L4
- Masseron, T., Johnson, J. A., Plez, B., et al. 2010, *A&A*, 509, A93
- Masseron, T., Plez, B., Van Eck, S., et al. 2014, *A&A*, 571, A47
- Matsuno, T., Amarsi, A. M., Carlos, M., & Nissen, P. E. 2024, *A&A*, 688, A72
- Matsuno, T., Aoki, W., & Suda, T. 2019, *ApJ*, 874, L35
- Meléndez, J., Ramírez, I., Karakas, A. I., et al. 2014, *ApJ*, 791, 14
- Myeong, G. C., Vasiliev, E., Iorio, G., Evans, N. W., & Belokurov, V. 2019, *MNRAS*, 488, 1235
- Nilsson, H. & Ivarsson, S. 2008, *A&A*, 492, 609, (NI)
- Nollett, K. M., Busso, M., & Wasserburg, G. J. 2003, *ApJ*, 582, 1036
- Nordlander, T. & Lind, K. 2017, *A&A*, 607, A75
- Panov, I. V., Korneev, I. Y., Rauscher, T., et al. 2010, *A&A*, 513, A61
- Placco, V. M., Frebel, A., Beers, T. C., & Stancliffe, R. J. 2014, *ApJ*, 797, 21
- Prantzos, N., Abia, C., Cristallo, S., Limongi, M., & Chieffi, A. 2020, *MNRAS*, 491, 1832
- Prša, A., Harmanec, P., Torres, G., et al. 2016, *AJ*, 152, 41
- Ram, R. S., Brooke, J. S. A., Bernath, P. F., Sneden, C., & Lucatello, S. 2014, *ApJS*, 211, 5
- Rochman, D., Koning, A., Goriely, S., & Hilaire, S. 2025, *Nucl. Phys. A*, 1053, 122951
- Roederer, I. U., Karakas, A. I., Pignatari, M., & Herwig, F. 2016, *ApJ*, 821, 37
- Ruchti, G. R., Bergemann, M., Serenelli, A., Casagrande, L., & Lind, K. 2013, *MNRAS*, 429, 126
- Ryabchikova, T., Piskunov, N., Kurucz, R. L., et al. 2015, *Phys. Scr.*, 90, 054005
- Sakari, C. M., Placco, V. M., Farrell, E. M., et al. 2018, *ApJ*, 868, 110
- Sbordone, L., Hansen, C. J., Monaco, L., et al. 2020, *A&A*, 641, A135
- Schlafly, E. F. & Finkbeiner, D. P. 2011, *ApJ*, 737, 103
- Semenova, E., Bergemann, M., Deal, M., et al. 2020, *A&A*, 643, A164
- Simmerer, J., Sneden, C., Cowan, J. J., et al. 2004, *ApJ*, 617, 1091
- Sitnova, T. M., Yakovleva, S. A., Belyaev, A. K., & Mashonkina, L. I. 2022, *MNRAS*, 515, 1510
- Skory, S., Weck, P. F., Stancil, P. C., & Kirby, K. 2003, *ApJS*, 148, 599
- Sneden, C., Cowan, J. J., & Gallino, R. 2008, *ARA&A*, 46, 241
- Sneden, C., Lucatello, S., Ram, R. S., Brooke, J. S. A., & Bernath, P. 2014, *ApJS*, 214, 26
- Spyrou, A., Mùcher, D., Denissenkov, P. A., et al. 2024, *Phys. Rev. Lett.*, 132, 202701
- Steffen, M., Ludwig, H.-G., Wedemeyer-Böhm, S., & Gallagher, A. 2023, *Linfor3D User Manual*
- Storm, N., Barklem, P. S., Yakovleva, S. A., et al. 2024, *A&A*, 683, A200
- Straniero, O., Gallino, R., & Cristallo, S. 2006, *Nucl. Phys. A*, 777, 311
- Vescovi, D. 2021, *Universe*, 8, 16
- Vescovi, D., Cristallo, S., Busso, M., & Liu, N. 2020, *ApJ*, 897, L25
- Vescovi, D., Cristallo, S., Palmerini, S., Abia, C., & Busso, M. 2021, *A&A*, 652, A100
- Wiedeking, M., Goriely, S., Guttormsen, M., et al. 2025, *Nature Reviews Physics*, 7, 696

Appendix A: Chemo-dynamic analysis

We computed the orbital parameters of TYC 6044-714-1 using the code GalPot¹⁵, with coordinates, proper motions, parallax, and radial velocity from *Gaia* DR3 (Gaia Collaboration et al. 2018) as inputs. Our algorithm follows that of Giribaldi & Smiljanic (2023) and Giribaldi et al. (2025a); we refer the reader to those papers for details.

We used the samples in the two papers above as references. These populations comprise stars from the Gaia-Enceladus merger (Helmi et al. 2018; Belokurov et al. 2018; Gallart et al. 2019), the Splash or heated thick disc (e.g., Belokurov et al. 2020; Bonaca et al. 2017; Di Matteo et al. 2019), Erebus (Giribaldi & Smiljanic 2023), and the metal-poor tail of the Milky Way (Giribaldi et al. 2025a). Figure A.1 shows the location of TYC 6044-714-1 and the concentrations of these populations in the Lindblad diagram, which plots space binding energy versus angular momentum (L_z). Among them, Gaia-Enceladus is the only population composed of stars formed outside the Milky Way. Erebus was initially hypothesised to be of external origin because most of its stars rotate contrary to the sense of the Galactic discs (called the Thamnos II population in Koppelman et al. 2019). Subsequently, the possibility that this and other retrograde populations formed in situ was reconsidered (Koppelman et al. 2020) based on numerical simulations (e.g., Jean-Baptiste et al. 2017). Using stellar ages, Giribaldi & Smiljanic (2023) demonstrated that Erebus stars are too old and metal-rich to originate from a satellite galaxy, thus confirming it as a Milky Way in situ population. This opens the possibility that other retrograde populations (e.g. Sequoia) may also have formed within the Milky Way.

We define the metal-poor tail as all stars with $[\text{Fe}/\text{H}] < -1.8$ dex. As the dispersion in Fig. A.1 shows, these are not orbitally linked. However, in the $[\text{Mg}/\text{Fe}]$ vs. $[\text{Fe}/\text{H}]$ plane, they form a knee-shaped sequence consistent with predictions from an evolutionary model of the Milky Way halo (see Fig. 10 in Giribaldi et al. 2025a), supporting the hypothesis of in situ formation.

Figure A.2 displays the stars of the populations described above in the $[\text{Mg}/\text{Fe}]$ versus $[\text{Fe}/\text{H}]$ plane. We note that these Mg abundances include 1D non-LTE corrections, which, according to Fig. A.7 in Giribaldi et al. (2025a), mainly¹⁶ affect the metal-poor tail. Based on comparisons with 3D non-LTE, they show that 1D non-LTE $[\text{Mg}/\text{Fe}]$ of stars with $[\text{Fe}/\text{H}] \lesssim -2$ dex requires a correction of about +0.2 dex. Therefore, in Fig. A.2, the trends of the metal-poor tail (solid line) and Erebus (dashed line) converge when Mg abundances approach their true values. Figure A.2 shows that TYC 6044-714-1 lies within the trend of the metal-poor tail in the $[\text{Mg}/\text{Fe}]$ versus $[\text{Fe}/\text{H}]$ plane, suggesting it is likely a star of the in situ halo. Figure A.1 shows that it moves as fast as the majority of stars in the discs, but in the opposite direction. Additionally, it is nearly as tightly bound to the Galaxy as the Sun, appearing near the border of the diagram.

Based on its retrograde orbit and moderate binding energy, the possibility that it belongs to the Sequoia population (Myeong et al. 2019) can be considered (see its proximity to the high-probability box in the figure). Chemically, Sequoia stars have been shown to form a sequence approximately 0.15 dex below that of Enceladus in the $[\text{Mg}/\text{Fe}]$ versus $[\text{Fe}/\text{H}]$ plane (Mat-

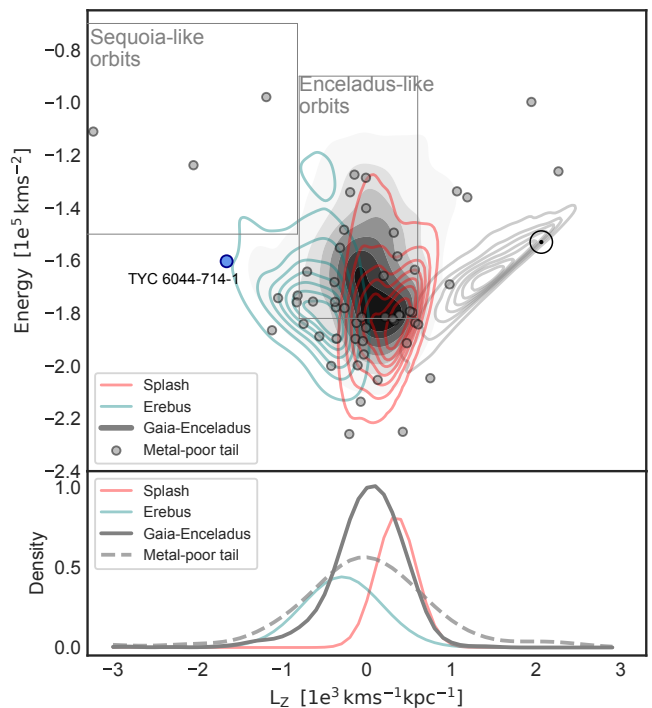


Fig. A.1. Linblad diagram. *Top panel:* Contours represent the cumulative distributions of the Erebus, Splash, and Gaia-Enceladus populations in Giribaldi & Smiljanic (2023); the latter is represented by the gray gradient. The cumulative distribution of the Milky Way discs is also shown at the right side, as well as the Sun's location represented by the symbol \odot . Gray circles represent the stars of the metal-poor tail in Giribaldi et al. (2025a). The boxes represent the high probability areas to find Gaia-Enceladus and Sequoia stars according to Massari et al. (2019). *Bottom panel:* Probability density distributions of the populations in the top panel, same colour coding is used.

suno et al. 2019). However, both the Sequoia and Enceladus sequences are clearly visible only for stars with $[\text{Fe}/\text{H}] > -2$ dex. This is likely due to evolutionary reasons. It has been estimated that the Milky Way was 4–5 times more massive than Gaia-Enceladus at the time of their merger (Helmi et al. 2018), while Gaia-Enceladus may have been about 10 times more massive than the hypothetical Sequoia progenitor (Myeong et al. 2019). A lower-mass galaxy is less efficient at forming stars, so the presence of Gaia-Enceladus and Sequoia stars is expected to be much less frequent than that of Milky Way in situ stars. The bias-corrected metallicity distribution function of Gaia-Enceladus (Bonifacio et al. 2021) confirms only a marginal fraction of stars with $[\text{Fe}/\text{H}] < -2$ dex, implying that the fraction of Sequoia stars is not expected to be higher. Based on this reasoning, we propose that TYC 6044-714-1 likely formed as a typical star in the Milky Way in situ halo more than 11 Gyr ago, as most dwarf stars in this population (Giribaldi et al. 2025a, Fig. 8).

Appendix B: Validation of surface gravity

Figure B.1 compares the surface gravities derived from the 1D non-LTE excitation balance of Fe lines (blue point) with those obtained from two other alternative methods. The application of those methods is described below, and corresponding results are listed in Table B.1. T_{eff} values in the figure were shifted to account for log g variations relative to our fiducial log $g = 1.70$ dex according to the grids in Fig. 5 of Giribaldi et al. (2023), i.e. $T_{\text{eff}} - 15$ K per log $g - 0.10$ dex.

¹⁵ <https://github.com/PaulMcMillan-Astro/GalPot>

¹⁶ Stars of Erebus, Splash, and Gaia-Enceladus are at the main sequence turn-off, where 3D non-LTE corrections to the 1D non-LTE Mg abundances significantly affect only stars with $[\text{Mg}/\text{Fe}] \lesssim 0.15$ at $[\text{Fe}/\text{H}] > -1.5$ dex (Matsuno et al. 2024).

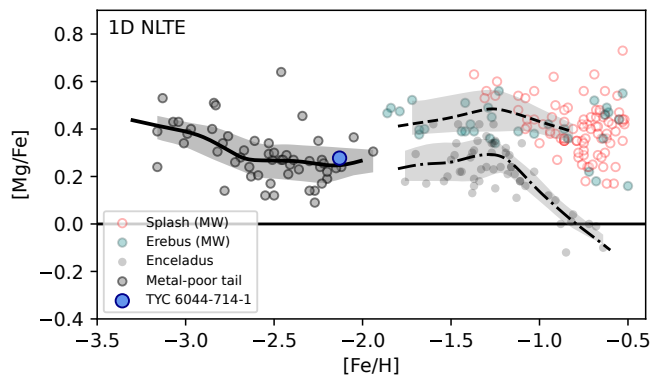


Fig. A.2. [Mg/Fe] vs. [Fe/H] diagram. Stars of the Erebus, Splash, Gaia-Enceladus, and the metal-poor tail populations in Giribaldi & Smiljanic (2023) and Giribaldi et al. (2025a) are represented according to the legends. Solid, dashed, and dash-dotted lines represent LOWESS regressions of each population except the Splash one.

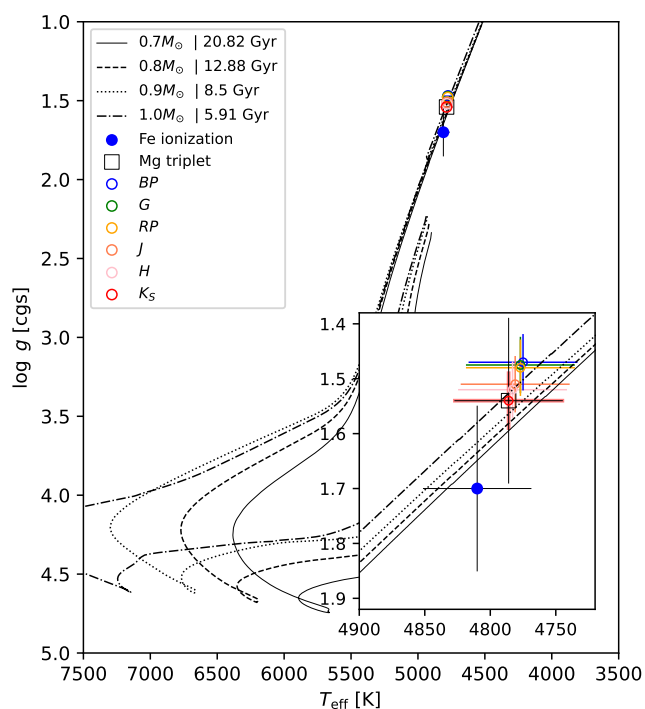


Fig. B.1. Kiel diagram of T_{eff} versus $\log g$. Surface gravities derived from three different methods are compared (see main text). FuNS evolutionary tracks for $[\text{Fe}/\text{H}] = -2.27$ dex and various initial masses are shown for reference. For each track, the age corresponding to the point closest to the observed $\log g$ is indicated (these values are independent of the method used to derive $\log g$). The inset shows a zoomed-in view of the region highlighted in the main panel.

Surface gravity from the *Mg triplet* was determined as described in Giribaldi et al. (2023) from the Mg triplet lines 5172.68 and 5183.60 Å, fixing T_{eff} , $[\text{Fe}/\text{H}]$, v_{mic} in Table 2, and $[\text{Mg}/\text{Fe}]$ in Table 3; see line fits in Fig. B.2. Errors relative to noise, T_{eff} , and $[\text{Mg}/\text{Fe}]$ errors are the most relevant, they account ± 0.10 , ± 0.10 , and ± 0.04 dex, respectively. We add them in quadrature to compute the total error given in the table.

Surface gravity from *Parallax* was determined via the classical relation

$$\log g = \log g_{\odot} + \log \frac{M}{M_{\odot}} + 4 \log \frac{T_{\text{eff}}}{T_{\text{eff}\odot}} + 0.4(M_{\text{bol}} - M_{\text{bol}\odot}) \quad (\text{B.1})$$

Table B.1. Surface gravity values from diverse methods

Method	$\log g$	magnitude	extinction	BC
Fe ionization	1.70 ± 0.15	—	—	—
Mg triplet	1.54 ± 0.15	—	—	—
Parallax (<i>BP</i>)	1.47 ± 0.05	12.326 ± 0.0006	0.120	-0.710
Parallax (<i>G</i>)	1.48 ± 0.05	11.056 ± 0.0002	0.094	-0.207
Parallax (<i>RP</i>)	1.48 ± 0.05	11.343 ± 0.0003	0.070	0.461
Parallax (<i>J</i>)	1.51 ± 0.05	9.59 ± 0.027	0.032	1.342
Parallax (<i>H</i>)	1.52 ± 0.05	9.009 ± 0.022	0.020	1.872
Parallax (<i>K_S</i>)	1.54 ± 0.05	8.926 ± 0.021	0.014	1.993

Notes. Last column indicates the bolometric correction.

where M is the stellar mass and M_{bol} is the bolometric magnitude. We adopted $0.80 \pm 0.05 M_{\odot}$ and the standard¹⁷ parameters $T_{\text{eff}\odot} = 5772$ K, $\log g = 4.44$ dex, and $M_{\text{bol}\odot} = 4.74$ (Prša et al. 2016). M_{bol} was computed from the Gaia and 2MASS (Cutri et al. 2003) magnitudes *BP*, *G*, *RP*, *J*, *H*, and *K_S* with the routine *bcutil.py*¹⁸ of Casagrande & Vandenberg (2018). Magnitudes were extinction corrected adopting the reddening value $E(B - V) = 0.0443$ from Schlafly & Finkbeiner (2011)¹⁹, which was transformed into the Gaia and 2MASS systems assuming the extinction law of Fitzpatrick (1999) as normalised per Schlafly & Finkbeiner (2011)²⁰. Absolute magnitudes were determined adopting a distance of 3022 ± 130 parsec from Bailer-Jones et al. (2021), which is based on Gaia 3D parallax and includes the zero-point correction $+0.021$ mas (Lindgren et al. 2021). The main sources of uncertainty are the distance, mass, T_{eff} , and magnitude errors, which account by 0.040, 0.026, 0.015, and 0.010, respectively; errors of the evolutionary model are neglected. Magnitudes, extinctions, and bolometric corrections are listed in Table B.1.

Figure B.1 shows that $\log g$ from Fe lines, Mg triplet, and parallax using 2MASS bands are compatible within 1σ errors. Equation B.1 implicitly assumes that the bolometric magnitude, as a proxy for luminosity, reflects the intrinsic properties of the star. In CEMP stars with strong blanketing, the flux can be redistributed toward redder wavelengths, decreasing magnitudes in the red bands and leading to systematic $\log g$ underestimates. However, the consistency of the outcomes of the methods implies that this effect is negligible for TYC 6044-714-1. A comparison with FuNS evolutionary tracks in Fig. B.1 indicates that the evolutionary path of a $\sim 0.8 M_{\odot}$ star provides an age diagnosis (13 Gyr) compatible to that in Sect. A, which suggests that TYC 6044-714-1 likely formed as a typical low-mass star more than 11 Gyr ago.

Appendix C: Abundances of niobium and thorium

We measured the Nb abundance from the Nb II lines at 3484.046 and 3740.72 Å (Fig. C.1). The $\log gf$ values of the lines (-1.060 and -0.310) were revised by Nilsson & Ivarsson (2008) and agree with former ones in Hannaford et al. (1985), which were used to successfully reproduce the solar meteoritic abundance $A(\text{Nb}) = 1.41$ dex (Anders & Ebihara 1982). Despite some blending, both lines yield consistent abundances (see Figure C.1). Biases arising from 1D LTE modelling and noise effects cannot be ruled out as contributing to an overestimation.

¹⁷ IAU 2015 RESOLUTION B3

¹⁸ <https://github.com/casaluca/bolometric-corrections>

¹⁹ Online tool <https://irsa.ipac.caltech.edu/applications/DUST/>

²⁰ Using the code *Colte* (Casagrande et al. 2021) at <https://github.com/casaluca/colte>.

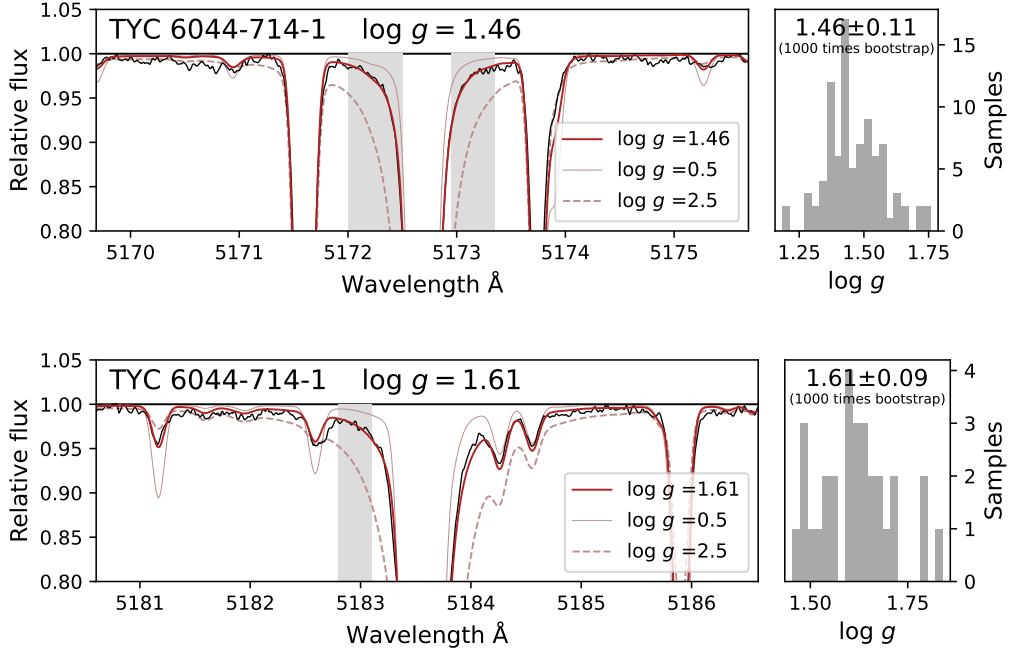


Fig. B.2. Mg triplet line fitting. The observed spectrum is shown in black, while the best-fitting synthetic 1D LTE profiles are overplotted as thicker red lines. The shaded regions indicate the wavelength intervals used in the fitting procedure. The right-hand panels display the distributions of $\log g$ values associated with the pixels within these regions. The most probable $\log g$ and its uncertainties are derived via bootstrapping.

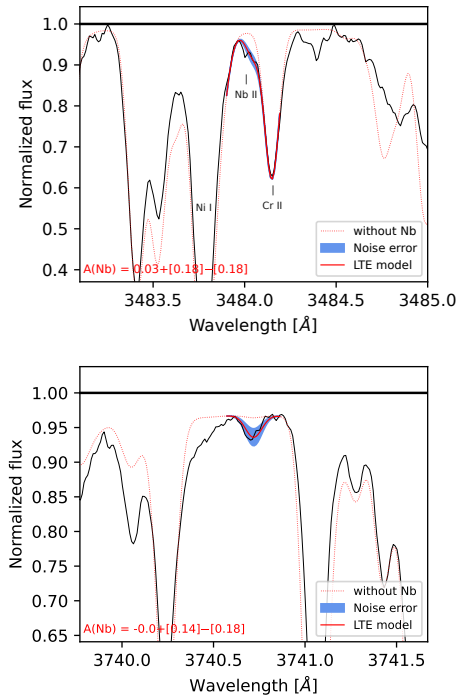


Fig. C.1. Nb spectral line synthesis. Symbols and colours are the same as to those in Fig. 3, but without 1D non-LTE line models.

The noise-related uncertainty per line is approximately 0.2 dex, which is adopted in Table 3 to account for potential biases. Elements with $38 \leq Z \leq 56$ may be distinctive between s+r and i+r+s scenarios (Sect. 5.2). Among the six elements in this range with detected lines, only Nb supports the latter, suggesting that its abundance may be affected by noise-induced bias.

We fitted the feature containing the Th II line at 4019.129 Å. In TYC 6044-714-1, the pseudo-continuum around this line is dominated by ^{12}CH (Figure C.2), therefore we normalised its spectrum to the synthetic flux using the blue and red limits at 4018.528 and 4019.629 Å. An unidentified line at 4019.28 Å was modelled with a Gaussian. Although the Th contribution is subtle, the high S/N allows a 2σ measurement, as seen in the residuals. The derived abundance depends on the proper modelling of the ^{13}CH feature near 4019.0 Å, the Ce II line at 4019.057 Å, and the ^{13}CH feature aligned with Th.

Appendix D: Extra Figures

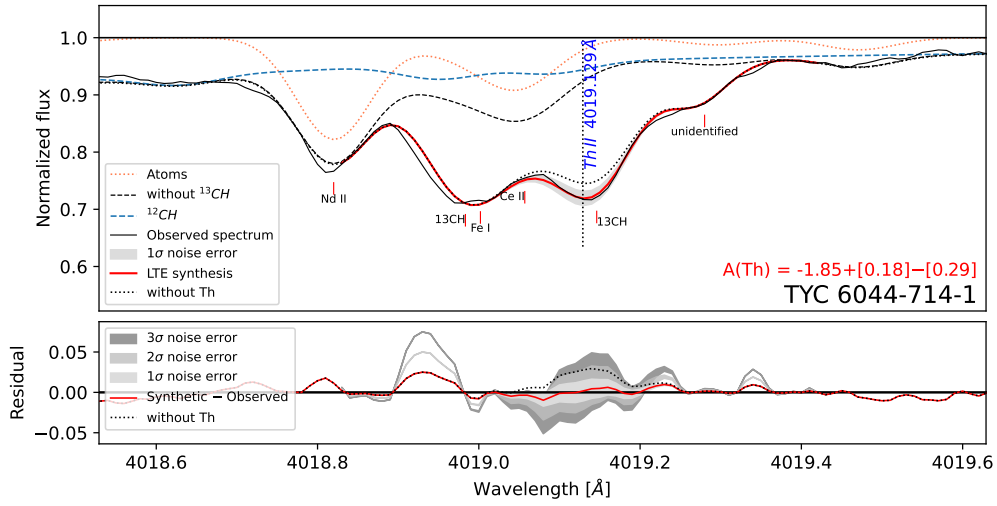


Fig. C.2. Modelling of the feature around the thorium line at $\lambda 4019.129 \text{ \AA}$. The core of the Th line is marked by the dotted vertical line. Lines of species with significant contributions to the feature are marked in the plot. The abundance retrieved from the spectral synthesis including all species (red solid line) is noted at the right bottom part of the plot. A synthetic spectrum without Th is represented by the dotted black line. The bottom panel displays residuals and 1, 2, and 3σ flux errors according to the legends.

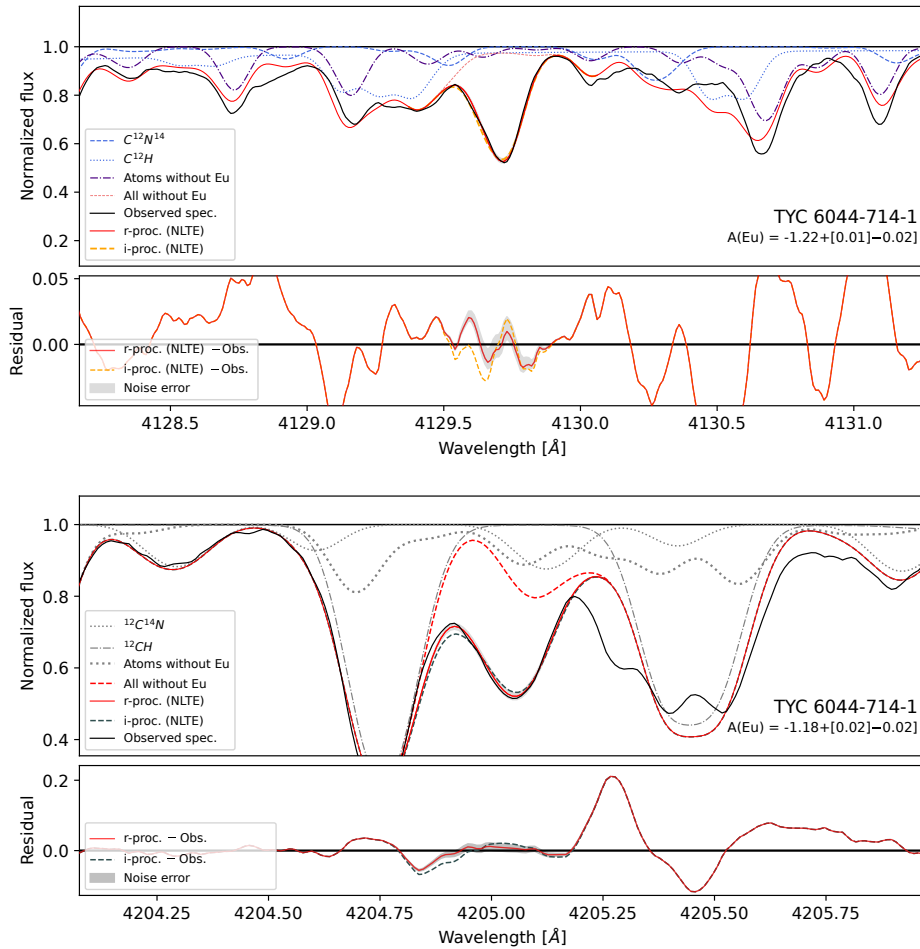


Fig. D.1. *Top panel:* Fit of the line at 4129 \AA . Line profiles from the r- and i-processes from the isotope fractions in Table 4 are represented in different colours as indicated in the legends. Flux contributions from CN and CH molecule features are also plotted. *Bottom panel:* Similar to top panel but for the line at 4205 \AA .

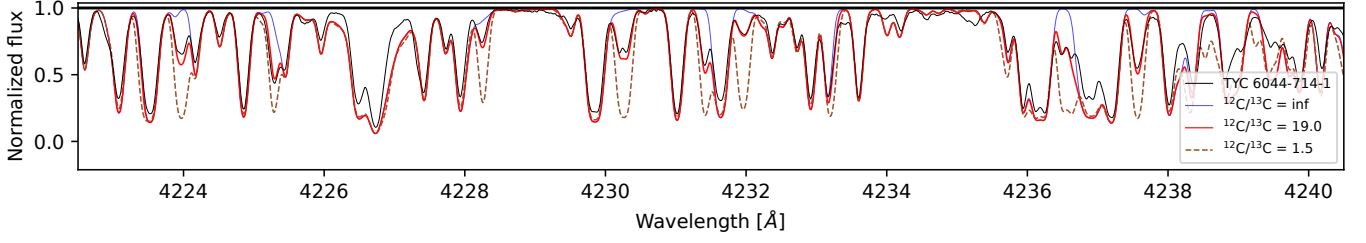


Fig. D.2. Section of the band used to determine $^{12}\text{C}/^{13}\text{C}$. The observational spectrum is represented by the black line. Synthetic with extreme $^{12}\text{C}/^{13}\text{C}$ fractions are represented by the red dashed and blue lines according to the legends. The synthetic spectrum most similar to the observational one is represented by the red solid line.

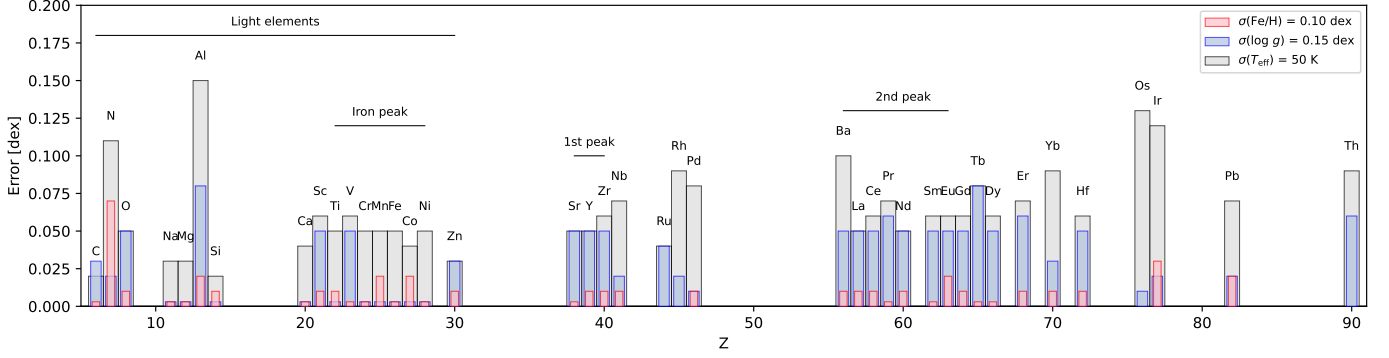


Fig. D.3. Elemental abundance variations induced by typical errors of T_{eff} , $\log g$, and $[\text{Fe}/\text{H}]$.

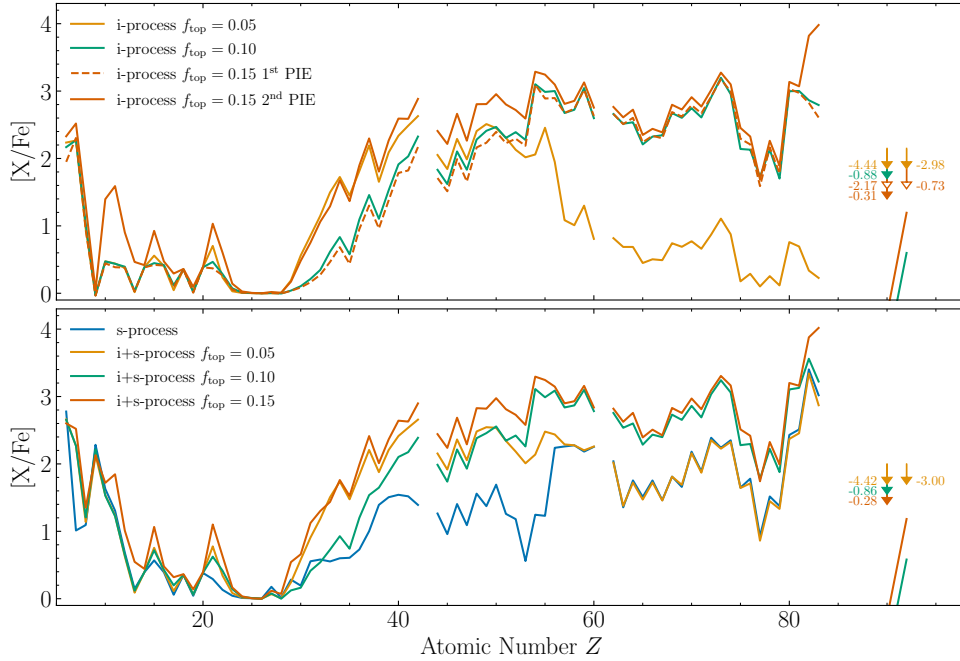


Fig. D.4. Final surface $[\text{X}/\text{Fe}]$ ratios predicted by our AGB models for a $1.5 M_{\odot}$ star at $[\text{Fe}/\text{H}] = -2.27$ (see text for details). *Upper panel:* surface abundance patterns obtained immediately after proton ingestion episodes (PIEs) for models with increasing overshooting efficiency at the top of the convective thermal pulse. The yellow, green, and orange curves correspond to $f_{\text{top}} = 0.05$, 0.10 , and 0.15 , respectively. For $f_{\text{top}} = 0.15$, two PIEs occur; the surface composition after the first PIE is shown as a dashed orange line, while the composition after the second PIE is shown as a solid orange line. *Lower panel:* final surface abundances after the full AGB evolution. The pure s-process model (blue line) results from 15 standard third dredge-up episodes associated with the formation of a ^{13}C pocket. Mixed i+s models are shown for increasing f_{top} values and include an initial enrichment caused by one or two PIEs and the associated deep third dredge-up, followed by standard s-process nucleosynthesis during the subsequent 12 thermal pulses. When computing elemental abundances, all unstable isotopes with half-lives shorter than 10 Myr are assumed to have fully decayed into their stable daughter nuclei.

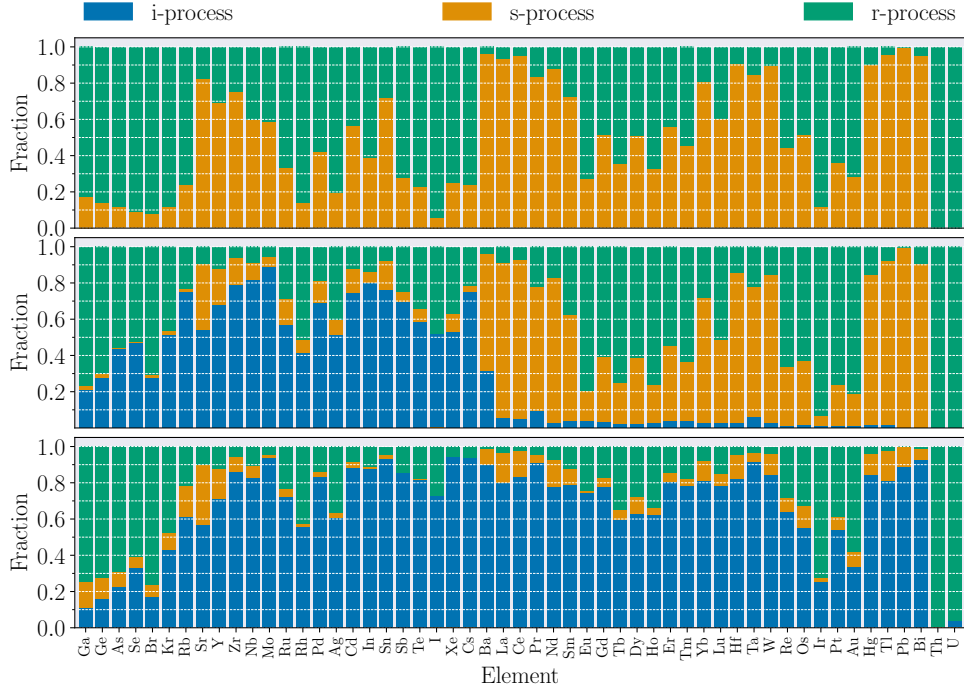


Fig. D.5. Nucleosynthesis fractions for the s+r model (upper panel) and for the mixed i+s+r models with $f_{\text{top}} = 0.05$ (middle panel) and 0.15 (lower panel), corresponding to the weakest and strongest i-process cases considered (see Fig. 8).

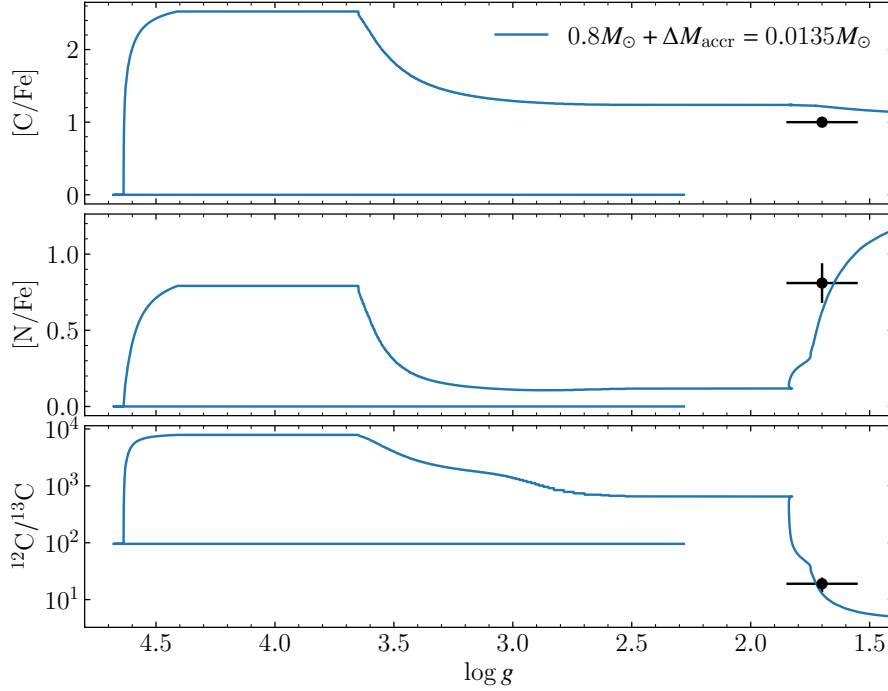


Fig. D.6. Evolution of surface $[\text{C}/\text{Fe}]$, $[\text{N}/\text{Fe}]$, and the $^{12}\text{C}/^{13}\text{C}$ ratio as a function of surface gravity ($\log g$) for the secondary star model. The star ($0.8 M_{\odot}$) is assumed to have accreted $0.0135 M_{\odot}$ from the primary AGB companion while on the Main Sequence, a mass required to match the dilution factor ($d_s = 0.027$) derived from the abundance fit of heavy elements (Fig. 8). The resulting $0.8135 M_{\odot}$ star then evolves through the RGB experiencing mass-loss. Non-convective extra-mixing ($v_{\text{mix}} = 1 \text{ cm s}^{-1}$, $T_{\text{mix}} = 23 \text{ MK}$) is implemented after the luminosity bump. The observed values for TYC 6044-714-1 at its current evolutionary stage are indicated by symbols.